FYS-3900

MASTER'S THESIS IN PHYSICS

A numerical study of planar elliptical antennas applied to ultrawideband (UWB) imaging of breast tissue

Sindre Holsbøe Brelum

June, 2008

FACULTY OF SCIENCE
Department of Physics and Technology
University of Tromsø

FYS-3900

MASTER'S THESIS IN PHYSICS

A numerical study of planar elliptical antennas applied to ultrawideband (UWB) imaging of breast tissue

Sindre Holsbøe Brelum

June, 2008

Abstract

The thesis discusses the possibility of using ultrawideband (UWB) radar to detect breast cancer. At the present time, X-ray mammography and ultrasound are the golden standard imaging techniques for detection and evaluation of breast cancer, but they both have their limitations. UWB radar utilizes the difference in dielectric properties between a tumor and the surrounding healthy tissue. By interpreting the reflected signals, it is possible to make a prediction on the localization of a tumor. The primary aim of this thesis is to use ultrawideband planar elliptical antennas in the detection of breast cancer, and investigate the use of the delay-and-sum beamforming technique applied on both the receiver (Rx) and transmitter (Tx).

At first, a description of the antenna and its basic characteristics are given, based on numerical simulations in CST Microwave Studio. This was done in order to get a better understanding of the antenna and its practicability. Then, models consisting of four identical antennas with a layer of fat between them and a tumor inside were constructed. Simulations were performed with the tumor placed on three different locations. The signal-to-clutter ratio is used as a measure of the systems overall performance. Some of the model parameters where changed in order to analyze the systems strengths and weaknesses. These parameters included the noise level, the size of the tumor, the active beamforming process on the transmitter and the difference in dielectric properties between the tumor and the healthy tissue.

General antenna parameters, such as the S_{11}-parameter, radiation patterns, group time delay and phase center were established. Initial indications show that the signal-to-clutter ratios generally increase with the use of the delay-and-sum beamforming technique on the transmitter and receiver, compared to only using it on the receiver. In addition to this, the models using Tx and Rx beamforming seems to have a higher tolerance with respect to changes in the model parameters than the models using only Rx beamforming.

Acknowledgements

I would like to thank my supervisor, Professor Svein Jacobsen, for sharing his knowledge and helping me explore and understand the world of ultrawideband signals. He has been very patient and supportive, and I've learned a lot from him. I also want to thank him for this possibility to study something that was completely unknown to me, with all the challenges that implied for the both of us.

Thanks to my family and relatives who have always believed in me. You have always been there for me, through all my ups and downs, and for that I am forever grateful. You may not have understood everything I've talked about for the last five years, but you have supported me in all the decisions I have taken in my life.

A big thanks goes to all my good friends, fellow students and teachers from the classes I attended at the University of Tromsø.

Thanks to you all.

Sindre Holsbøe Brelum
Tromsø, Norway, June 2008.

Contents

Chapter 1

Introduction

1.1 Medical rationale

In the human body, tissue and organs consist of different cells. At one point in time a cell dies, but in order to maintain the size of the organs, new cells must be formed to replace the dead ones. New cells are formed by cell division. But, if cells start to divide faster than the the old ones die, these new cells can form a tumor. The tumor can be either benign or malignant. Benign tumors do not grow into the tissue around it, or spread to other parts of the body. However, a malignant tumor can destroy the surrounding tissue. Cells can also loosen from the original (primary tumor) and spread with the blood- or lymph system. These cells are called secondary tumors. The forming of these secondary tumors is called metastasis [1].

The breast consists mainly of fat and glandular tissue and it is most common that a tumor is formed in the latter parts. Breast cancer can be divided into different stages, depending on size of the tumor and whether or not it has formed secondary tumors. Identifying the cancer stage is important in selecting the proper treatment. The staging system ranges from Stage 0 to Stage IV. In the stages 0 - II, the tumor is smaller than 5 cm in diameter and has not spread to distant sites of the body. Breast cancer in Stage III may be larger than 5 cm and has spread to tissues near the breast, such as the skin or chest wall and also to the axillary lymph nodes or internal mammary nodes. Stage IV breast cancer is diagnosed when the primary cancer has spread out of the breast to other parts of the body, such as bone, lung, liver or brain. The treatment of breast cancer at this stage is mainly focused on extending survival time and relieving symptoms for the patients.

Based on the stage of the breast cancer for a patient, physicians are able to predict the survival rate. Often used is the five-year survival rate, which refers to the average number of patients who are still alive five years after being diagnosed with a specific stage of breast cancer. After seven years, the survival rates will decrease for each stage. It is important to remember that these survival rates are based on averages and may vary depending on the individual medical situation etc. An overview of five-year survival rates for some of the different breast cancer stages is given in Table 1.1 [2, 3].

Stage	5-year Relative Survival Rate
0	100 %
I	100 %
II A	92 %
II B	81 %
III A	67 %
III B	54 %
IV	20 %

Table 1.1: Five-year survival rates for some breast cancer stages [3].

As seen in Table 1.1, the detection at an early stage is important for long-time survival and good life quality for breast cancer patients. Today, X-ray mammography and ultrasound are the standard imaging techniques for detection and evaluation of breast cancer [4]. Mammography is the application of low-energy X rays. In an X-ray tube, a heated filament releases electrons that are accelerated onto a target because a high voltage is applied across it. This stream of electrons is called tube current. X-rays are produced when the electrons interact with the target. A vacuum is maintained inside the tube, so that the electrons does not interact with other molecules. The energy of the emerging X-rays are dependent of the voltage between the filament and the target. In mammography, the voltage applied is low and the target is often molybdenum. When bombarded with electrons, this target produces X-rays with an approximate energy of 17 and 19 keV [5].

Although there has been progress in mammography imaging, this method has its limitations. It has been estimated that 4%-34% of all breast cancers are missed by common mammography [6], and almost 70% of all cases are actually benign [7]. The false-negative rates are especially high when diagnosing very dense breasts or breasts with implants. In a study of 18 patients with implants and breast cancer, mammography showed an abnormality in only one patient [8]. Also, it is commonly known that the mammogram examination can be uncomfortable to the patient. The breast is compressed during the examination, and the patient is also exposed to low levels of ionizing radiation.

Because of the many limitations of mammography, breast ultrasound is also used in the diagnosing process. An ultrasonic wave has per definition a frequency higher than 20 kHz. When used in clinical diagnosis, the frequencies of the ultrasonic waves are between 1 and 20 MHz. There are three ways of presenting the ultrasound images: Amplitude (A-mode), brightness (B-mode) and motion (M-mode) [5]. The B-mode is the most commonly used in breast ultrasound. Transducers transmits short bursts of ultrasonic energy, followed by a listening period were the echoes from the ultrasonic waves are recorded. The amplitude of the echoes are used to control the brightness of the picture. The skin is highly reflective and is shown as a bright line on the image, while fat cause low-level echoes and appears dark. Breast lesions are often darker than the surrounding tissue. The echoes received from different directions are combined to form a 2D image of the breast. When these images are displayed in rapid succession, real-time imaging is possible. A limitation of breast ultrasound is its inability to detect small lesions. This is mainly due to the complex structure of the breast and noise in the image caused by speckle phenomena. In addition, it is difficult to separate a benign lesion from a malignant. Usually biopsy is needed to make this decision, which can result in unnecessary stress and cost for the patient [9].

MRI of the breast is currently used as an adjunct to mammography and ultrasound. The primary source of MRI signals is the mobile protons in hydrogen atoms, which is found in water and fat. The hydrogen nucleus contains one charged proton that spins and creates an electromagnetic field with the characteristics of a magnetic dipole. It is known from quantum mechanics that when an atom is placed in a strong external magnetic field, the nucleus can have two spin states or energy levels. Most of the nuclei prefers the lower energy level. When electromagnetic radiation in the radio frequency range is applied, nuclei can absorb energy and thus rise to a higher energy level. As these nuclei relax back to their lower state, energy will be radiated, and it is this energy that is the source of MRI signal [10]. Often, a substance is injected into the body in order to enhance tissue contrast. These substances are called contrast agents [5]. Contrast-enhanced MRI has demonstrated a sensitivity of 94% - 100% in the detection of breast cancer [11]. In a study [12] that included 192 asymptomatic women, the accuracy of MRI was found to be significantly higher than that of conventional imaging. Mammography found 3 of 9 breast cancers (33% sensitivity), while MRI correctly classified and locally staged all nine cancers (100% sesitivity). However, a major limitation of contrast-enhanced breast MRI is its relatively low specificity which rages from 37% to 97% [13]. Also, both cancer and benign lesions may enhance after administration of contrast material, making it difficult to separate the two. Other limitations include the lack of MRI-guided localization and biopsy technology and the fact that the method is fearly cost-expensive [14].

1.2 Ultrawideband radar technology

Ultrawideband (UWB) radar transmission is a technology for transmitting and receiving signals over a large bandwidth by the use of one or more antennas. A common narrowband radar has a relative bandwidth that is much less than one: $\frac{\Delta f}{f_0} \ll 1$, while a UWB radar has a relative bandwidth that is in the order of, or even grater than, one : $\frac{\Delta f}{f_0} \approx 1$. In 2002, the federal communications commission (FCC), authorized the unlicensed use of UWB in the 3.1-10.6 GHz band [15]. UWB radar technology is currently used in many subsurface sensing applications, such as detecting unexploded land mines, examining archeology sites and studying groundwater [16].

A UWB system is based on an antenna which radiates bursts of microwave energy with extremely short duration, in order of nanoseconds or even sub nanoseconds. The transmitted waves penetrate the material of interest and are scattered by any targets that has a mismatch in dielectric properties. The scattered signal is recorded by one or several receiving antennas. In recent years, UWB radar has been introduced to medical applications, especially for the detection of malignant tumors in the female breast [17].

Several studies in the past two decades indicate that the contrast in dielectric properties between malignant and normal breast tissue in the microwave frequency range is greater than 2:1 [18] - [20]. This good contrast is the basis for active microwave imaging technique. The use of frequencies in the microwave range for medical application is not randomly picked. From 1 G Hz to 10 G Hz there is a balance between spatial resolution (better at higher frequencies) and penetration depth (better at lower frequencies). Three different kinds of active microwave imaging techniques have been proposed for breast cancer detection: hybrid microwave-induced acoustic imaging [21, 22], microwave tomography [23] - [27] and ultrawideband radar techniques [28] - [34].

The hybrid model transmits microwave signals into the breast, thus heating the tumor. Ultrasound transducers detect the pressure waves caused by the tumor expansion. The received waveforms can be used to determine the dielectric-properties distribution inside the breast [35].

The goal in tomography is to recover a complete profile of the dielectric properties in the breast, using narrowband signals. A promising two-dimensional clinical system for microwave breast imaging has been developed [24], and progress has also been made in the three-dimensional case [26, 36].

The radar technique does not try to reconstruct the complete profile, but instead seek to identify and locate significant backscattered energy. The scattered signals provides information about the existence and localization of tumors as a function of spatial location in the breast. Microwave Imaging via Space-Time (MIST) beamforming is one method that has been presented in the literature for breast cancer detection [33]. In the space-time beamformer, each antenna in an array transmits a low-power UWB pulse into the breast and records the backscatter. To prevent cluttering, the beamformer spatially focuses the backscatter signals [37].

One major advantage for UWB imaging is its potential to separate malignant from benign tissue. Since benign tissue has almost the same dielectric properties as normal breast tissue, the scatter from these tumors will have a low intensity compared to the scatter from a malignant tumor, which has a significant difference in dielectric properties [17]. In addition to this method, UWB imaging can also use spectral and polarization signatures to make a distinction between malignant and benign tissue [29].

However, the UWB radar faces several challenges. The scattering response from the skin-to-breast interface is larger (at least one order of magnitude) than any tumor response. The tumor response is further concealed by clutter due to the heterogeneity of the breast, i.e. the natural variation on dielectric properties of breast tissue. Suppression or removal of these responses are necessary in order to have a minimum distortion of the tumor response. More practical problems include design and fabrication of the UWB antenna, the size of the aperture and scan time [17].

Chapter 2

Methodology

2.1 Transmission line theory

2.1.1 Circuit model and wave propagation

A transmission line can be up to many wavelengths in size, as opposed to the case of traditional circuit analysis where the physical dimensions of the network is assumed to be much smaller than the electrical wavelength. Due to this, the voltages and currents can vary in magnitude and phase over the network length. A transmission line is often represented as a two-wire line, as seen on Fig. 2.1a. This transmission line of infinitesimal length Δz, can be modeled as a lumped element circuit, as shown on Fig. 2.1b, where R, L, G and C are defined as follows:

R = series resistance per unit length, for both conductors, in Ω/m.

L = series inductance per unit length, for both conductors, in H/m.

G = shunt conductance per unit length, in S/m.

C = shunt capacitance per unit length, in F/m.

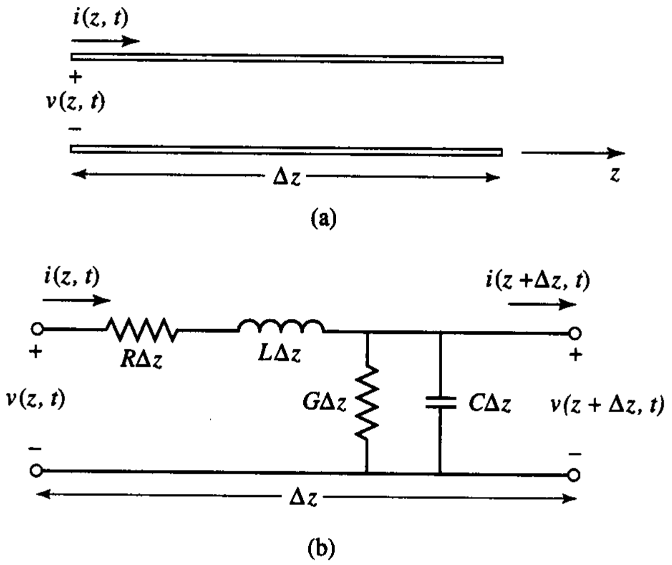

Figure 2.1: Schematic of a transmission line [38]. (a) Voltage and current definitions. (b) Lumped-element equivalent circuit.

The series inductance represents the total self-inductance of the two conductors, and the shunt capacitance is due to the nearness of the two conductors. The series resistance represents the resistance due to the finite conductivity of the conductors, and the shunt conductance is due to dielectric loss in the material between the conductors.

The time domain form of the transmission line equations, also called telegrapher equations, is as follows:

$$\frac{\partial v(z,t)}{\partial z} = -Ri(z,t) - L\frac{\partial i(z,t)}{\partial t}, \tag{2.1.1}$$

$$\frac{\partial i(z,t)}{\partial z} = -Gv(z,t) - C\frac{\partial v(z,t)}{\partial t}. \tag{2.1.2}$$

Assuming a sinusoidal steady state condition, with cosine-based phasors and a complex propagation constant defined as

$$\begin{aligned} \gamma &= \alpha + j\beta \\ &= \sqrt{(R + j\omega L)(G + j\omega C)}. \end{aligned} \tag{2.1.3}$$

Equations (2.1.1) and (2.1.2) can then be written on the form

$$\frac{d^2V(z)}{dz^2} - \gamma^2 V(z) = 0, \tag{2.1.4}$$

$$\frac{d^2I(z)}{dz^2} - \gamma^2 I(z) = 0. \tag{2.1.5}$$

Solutions of these differential equations are on the form

$$V(z) = V_0^+ e^{-\gamma z} + V_0^- e^{\gamma z}, \tag{2.1.6}$$

$$I(z) = I_0^+ e^{-\gamma z} + I_0^- e^{\gamma z}. \tag{2.1.7}$$

The $e^{-\gamma z}$ term represents wave propagation in the +z direction, and the $e^{\gamma z}$ term represents wave propagation in the -z direction.

The characteristic impedance, Z_0, is defined as

$$Z_0 = \frac{R + j\omega L}{\gamma} = \sqrt{\frac{R + j\omega L}{G + j\omega C}}. \tag{2.1.8}$$

The characteristic impedance can be used to relate the voltage and current on the transmission line as

$$\frac{V_0^+}{I_0^+} = Z_0 = \frac{-V_0^-}{I_0^-}. \tag{2.1.9}$$

For a lossless transmission line, we have $R = G = 0$ which reduces the characteristic impedance to

$$Z_0 = \sqrt{\frac{L}{C}}. \tag{2.1.10}$$

We also get general solutions for the voltage and current in this case

$$V(z) = V_0^+ e^{-j\beta z} + V_0^- e^{j\beta z}, \tag{2.1.11}$$

$$I(z) = \frac{V_0^+}{Z_0} e^{-j\beta z} - \frac{V_0^-}{Z_0} e^{j\beta z}. \tag{2.1.12}$$

Now, assume an incident wave on the form $V_0^+ e^{-j\beta z}$ is transmitted onto a lossless transmission line terminated in an arbitrary load Z_L. The ratio of voltage to current is Z_0 on the line and Z_L at the load. To satisfy this condition, a reflected wave must be excited with an appropriate amplitude. The voltage and current on the line is expressed in Eq. (2.1.11)-(2.1.12). The total voltage and current at the load (z=0) are related by the total load impedance, so that

$$Z_L = \frac{V(0)}{I(0)} = \frac{V_0^+ + V_0^-}{V_0^+ - V_0^-} Z_0 \tag{2.1.13}$$

Solving for V_0^-, and we get

$$V_0^- = \frac{Z_L - Z_0}{Z_L + Z_0} V_0^+ \tag{2.1.14}$$

The voltage reflection coefficient, Γ, is defined as the amplitude of the reflected voltage wave normalized to the amplitude of the incident voltage wave:

$$\Gamma = \frac{V_0^-}{V_0^+} = \frac{Z_L - Z_0}{Z_L + Z_0} \tag{2.1.15}$$

Γ is a complex number and Γ=0 indicates no reflected wave. To obtain this, the load impedance must be equal to the characteristic impedance of the transmission line, $Z_L = Z_0$. Such a load is said to be matched to the line, since there is no reflection of the incident wave. When the load is mismatched, not all available power is delivered to the load. This loss is called return loss (RL) and is defined in dB as

$$RL = -20 \log |\Gamma| \, dB, \tag{2.1.16}$$

so that a matched load (Γ=0) has a return loss of ∞ (no reflected power), and total reflection of the incident wave ($|\Gamma|$=1) has a return loss of 0 dB (all incident power is reflected).

In the case where the load is mismatched to the line, reflected waves leads to standing waves where the magnitude of the voltage on the line is not constant. A measure of the line mismatch is a parameter called standing wave ratio, SWR, or voltage standing wave ratio, VSWR,

$$SWR = \frac{1 + |\Gamma|}{1 - |\Gamma|}. \tag{2.1.17}$$

It is seen that 1$\leq$ SWR $\geq \infty$, where SWR = 1 implies a matched load. Different standing waves are seen on Fig. 2.2.

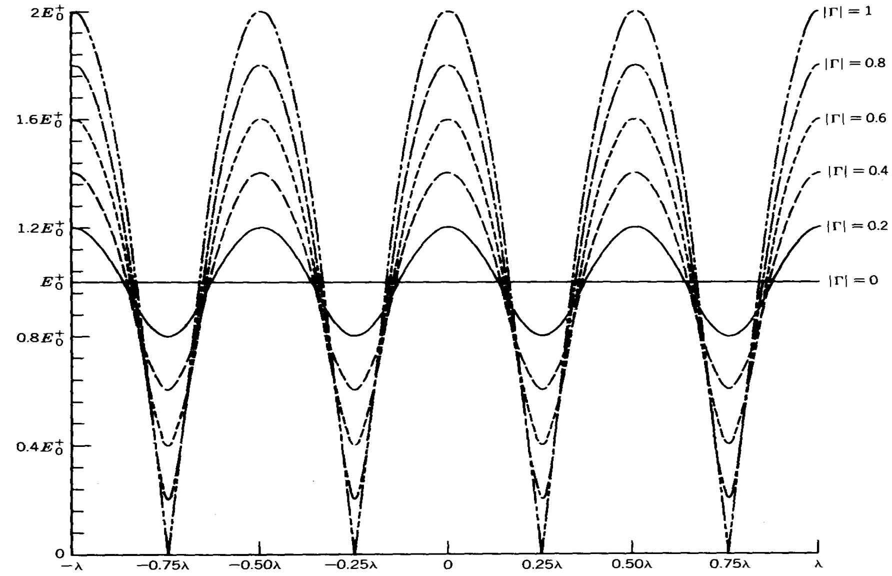

Figure 2.2: Standing wave pattern as a function of distance for a plane wave with different reflection coefficients $|\Gamma|$ [39].

We have seen that the voltage amplitude may vary with position on a mismatched line. Therefore, the impedance seen looking into this line must also vary with position. This input impedance is expressed in the transmission line impedance equation stated below:

$$Z_{in} = Z_0 \frac{Z_L + jZ_0 \tan \beta l}{Z_0 + jZ_L \tan \beta l} \tag{2.1.18}$$

A special case of the input impedance is when the line is a quarter-wavelength long, or in general, l=λ/4+nλ/2, for n=1,2,3... . This gives us the quarter-wave transformer [38]

$$Z_{in} = \frac{Z_0^2}{Z_L} \tag{2.1.19}$$

Fig. 2.3 shows a voltage transmission system with a series mode interference. A noise voltage, V_{SM}, is in series with the measurement signal voltage E_{Th}.

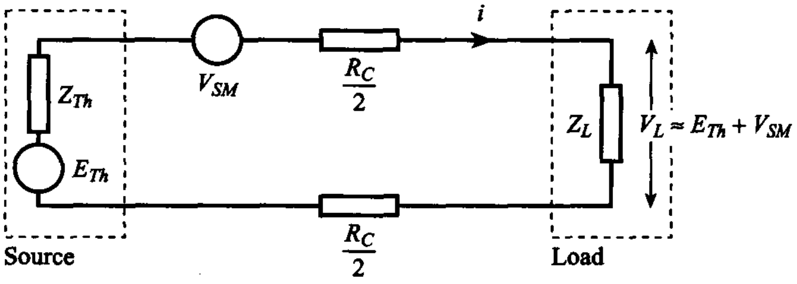

Figure 2.3: Effects of noise on a voltage transmission circuit [40].

The current through the load is

$$i = \frac{E_{Th} + V_{SM}}{Z_{Th} + R_C + Z_L} \tag{2.1.20}$$

The corresponding voltage over the load is

$$V_L = \frac{Z_L}{Z_{Th} + R_C + Z_L} \left(E_{Th} + V_{SM}\right) \tag{2.1.21}$$

To obtain maximum voltage transfer to the load, we set $Z_L \gg R_C + Z_{Th}$ and Eq. (2.1.21) becomes

$$V_L = E_{Th} + V_{SM} \tag{2.1.22}$$

This means that all of the noise voltage is across the load. Now we can define the signal-to-noise ratio (SNR) in decibels as

$$SNR(dB) = 20log_{10}\left(\frac{E_{Th}}{V_{SM}}\right) \tag{2.1.23}$$

where E_{Th} and V_{SM} are root mean square values that can be found by using the following formula [40]

$$y_{rms} = \sqrt{\frac{1}{N}\sum_{i=1}^{N} y_i^2} \tag{2.1.24}$$

In addition to the SNR, the signal-to-clutter (S/C) ratio can be defined as the ratio of the maximum tumor response to the maximum response not caused by the tumor,

$$S/C = \frac{maximum\ tumor\ response}{maximum\ response\ not\ caused\ by\ the\ tumor} = \frac{S}{C}\ [35]. \tag{2.1.25}$$

From elementary physics, we know that the velocity of an electromagnetic wave in vacuum is a constant, denoted c. When traveling in a dispersive medium or through a dispersive wave system, the wave velocity changes and becomes dependent on the medium in which the wave travels through. In this case, the wave velocity can be written as [38]

$$v = 1/\sqrt{\mu\epsilon} \tag{2.1.26}$$

Given steady-state conditions, the phase velocity can be introduced. The phase velocity describes the the velocity where a constant phase point appears to move along the medium or system. The phase velocity does not need to be the same for each frequency component of a wave. Different components of the wave may therefore travel with different speeds and give rise to phase distortion of the waveform. This phase velocity, v_p, is given by the following formula

$$v_p = \omega/\beta \tag{2.1.27}$$

Since the system is in a steady-state condition, no information is transmitted. Therefore, the phase velocity is not associated with any physical properties. This explains why, in some dispersive media and at certain frequency bands, the fact that the phase velocity may be larger than c does not violate Einstein's theory of special relativity.

The group velocity is the velocity of the envelope of the wave train. It is this velocity that transports the information in the signal. The group velocity, v_g, is defined as

$$v_g = \frac{d\omega}{dk}|_{k_0} \tag{2.1.28}$$

where k is the wave number. When k is complex, $k = \beta - j\alpha$, the group velocity becomes [41]

$$v_g = \frac{d\omega}{d\beta}|_{\beta_0} = \frac{1}{d\beta/d\omega|_{\beta_0}} \tag{2.1.29}$$

2.1.2 Microstrip antenna

Deschamps was the first one who proposed the concept of the microstrip antennas in 1953 [42]. However, it was not until the 1970s that Munson [43, 44] and Howell [45] developed the first practical antennas. The feeding technique has a major influence on the characteristics of the antenna, and is therefore an important design parameter. A microstrip antenna can be excited indirectly using electromagnetic coupling or aperture coupling and a coplanar waveguide feed. Directly excitation of the antenna includes a coaxial line or a microstrip line [46]. A microstrip line is a planar transmission line that can be fabricated by a photolithographic process. As we can see on Fig. 2.4a, a microstrip line consists of a conductor with width W printed on a thin, grounded dielectric substrate of thickness d and a relative permittivity of ϵ_r. Fig. 2.4b shows a sketch of the field lines on the same microstrip line.

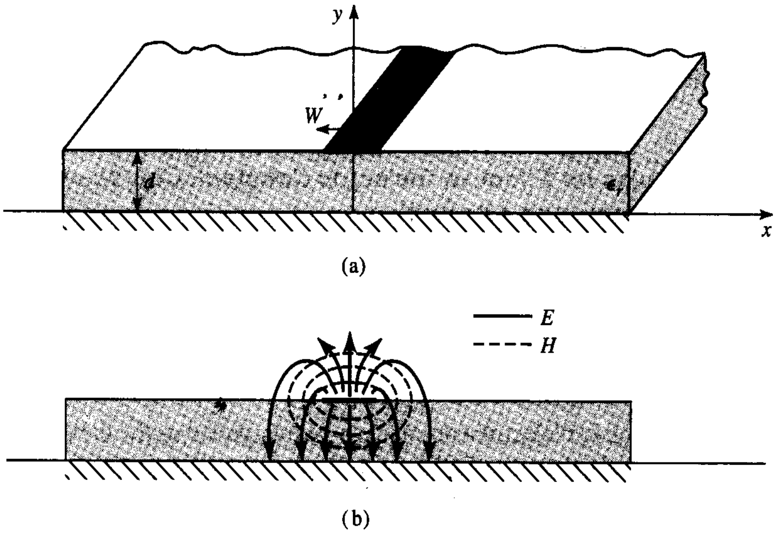

Figure 2.4: A figure showing a microstrip line [38]. (a) The geometry. (b) Electric and magnetic field lines.

As we can see on Fig. 2.4b, the field lines enter both air and the dielectric material. Therefore, an effective dielectric constant, ϵ_e, is introduced and can be interpreted as the dielectric constant of a homogeneous medium that replaces the air and dielectric part of the microstrip. This effective dielectric constant is given by:

$$\epsilon_e = \frac{\epsilon_r + 1}{2} + \frac{\epsilon_r - 1}{2} \frac{1}{\sqrt{1 + 12d/W}}, \tag{2.1.30}$$

Due to this fact, the effective dielectric constant satisfies the following relation:

$$1 < \epsilon_e < \epsilon_r.$$

The phase velocity and the propagation constant for a microstrip line are stated below:

$$v_p = \frac{c}{\sqrt{\epsilon_e}}, \tag{2.1.31}$$

$$\beta = k_0 \sqrt{\epsilon_e}. \tag{2.1.32}$$

Given the dimensions of a microstrip line, the characteristic impedance can be found through the following equations

$$Z_0 = \frac{60}{\sqrt{\epsilon_e}} \ln\left(\frac{8d}{W} + \frac{W}{4d}\right) \; for \; W/d \leq 1 \tag{2.1.33}$$

$$Z_0 = \frac{120\pi}{\sqrt{\epsilon_e}\left[W/d + 1,393 + 0,667 \ln\left(W/d + 1,444\right)\right]} \; for \; W/d \geq 1 \tag{2.1.34}$$

For a given characteristc impedance Z_0 and a dielectric constant ϵ_r, the W/d ratio can be calculated as

$$\frac{W}{d} = \frac{8e^A}{e^{2A} - 2} \; for \; W/d < 2 \tag{2.1.35}$$

$$\frac{W}{d} = \frac{2}{\pi}\left[B - 1 - \ln(2B-1) + \frac{\epsilon_r - 1}{2\epsilon_r}\left\{\ln(B-1) + 0,39 - \frac{0,61}{\epsilon_r}\right\}\right] \; for \; W/d > 2 \tag{2.1.36}$$

where

$$A = \tfrac{Z_0}{60}\sqrt{\tfrac{\epsilon_r+1}{2}} + \tfrac{\epsilon_r-1}{\epsilon_r+1}(0,23 + \tfrac{0,11}{\epsilon_r})$$

$$B = \tfrac{377\pi}{2Z_0\sqrt{\epsilon_r}}$$

The attenuation due to dielectric loss can be determined by

$$\alpha_d = \frac{k_0 \epsilon_r (\epsilon_e - 1) \tan\delta}{2\sqrt{\epsilon_e}(\epsilon_r - 1)} \; Np/m, \tag{2.1.37}$$

and the attenuation due to conductor loss is

$$\alpha_c = \frac{R_s}{Z_0 W} \; Np/m. \tag{2.1.38}$$

where $R_s = \sqrt{\omega\mu_0/2\sigma}$ is the surface resistivity of the conductor.

2.1.3 Microwave network analysis

The concept of impedance was first introduced in the nineteenth century by Oliver Heaviside. He used the term to describe the complex ratio V/I in AC circuits consisting of resistors, inductors and capacitors. It was later applied to transmission lines and is regarded as a link between field theory and transmission line or circuit theory.

Consider an arbitrary N-port microwave network. A specific point on the nth port is defined as a terminal plane, t_n, along with voltages and currents for the incident (V_n^+, I_n^+) and reflected (V_n^-, I_n^-) waves. Looking at the nth terminal plane, the total voltage and current is given by

$$V_n = V_n^+ + V_n^-, \tag{2.1.39}$$

$$I_n = I_n^+ + I_n^-, \tag{2.1.40}$$

as seen from Eq. (2.1.11) and (2.1.12) when z=0. The impedance matrix [Z] relates these voltages and currents:

$$\begin{pmatrix} V_1 \\ V_2 \\ \vdots \\ V_N \end{pmatrix} = \begin{pmatrix} Z_{11} & Z_{12} & \cdots & Z_{1N} \\ Z_{21} & & & \vdots \\ \vdots & & & \\ Z_{N1} & \cdots & & Z_{NN} \end{pmatrix} \begin{pmatrix} I_1 \\ I_2 \\ \vdots \\ I_N \end{pmatrix}, \tag{2.1.41}$$

or on matrix form as $[V] = [Z][I]$. We can also define the admittance matrix [Y] as

$$\begin{pmatrix} I_1 \\ I_2 \\ \vdots \\ I_N \end{pmatrix} = \begin{pmatrix} Y_{11} & Z_{12} & \cdots & Y_{1N} \\ Y_{21} & & & \vdots \\ \vdots & & & \\ Y_{N1} & \cdots & & Y_{NN} \end{pmatrix} \begin{pmatrix} V_1 \\ V_2 \\ \vdots \\ V_N \end{pmatrix}, \tag{2.1.42}$$

which on matrix form is $[I] = [Y][V]$.

It is seen that the [Z] and [Y] matrices are inverse of each other: $[Y] = [Z]^{-1}$. The elements of the [Z] and [Y] matrices can be found as

$$Z_{ij} = \frac{V_i}{I_j}, \tag{2.1.43}$$

and

$$Y_{ij} = \frac{I_i}{V_j}. \tag{2.1.44}$$

Below is a summary of different types of impedance:

- $Z_0 = 1/Y_0 = \sqrt{L/C}$=characteristic impedance. Characteristic impedance is, as mentioned before, the ratio of voltage to current for a wave on a transmission line.
- $\eta = \sqrt{\mu/\epsilon}$=intrinsic impedance of the medium. This impedance is equal to the wave impedance for plane waves and is only depending on the material parameters of the medium.
- $Z_w = E_t/H_t = 1/Y_w$=wave impedance. This impedance is depending on the type of wave. Each type of wave has different impedances, depending on the type of line or guide, the material and the operating frequency.

The scattering matrix , [S] , relates the voltage waves incident on the ports to those reflected from the ports, and is often measured directly with a network analyzer. Mathematically, the scattering matrix is written as:

$$\begin{pmatrix} V_1^- \\ V_2^- \\ \vdots \\ V_N^- \end{pmatrix} = \begin{pmatrix} S_{11} & S_{12} & \cdots & S_{1N} \\ S_{21} & & & \vdots \\ \vdots & & & \\ S_{N1} & \cdots & & S_{NN} \end{pmatrix} \begin{pmatrix} V_1^+ \\ V_2^+ \\ \vdots \\ V_N^+ \end{pmatrix}, \tag{2.1.45}$$

or on matrix form $[V^-] = [S][V^+]$.

A specific element of the [S] matrix can be determined by the following formula

$$S_{ij} = \frac{V_i^-}{V_j^+} \tag{2.1.46}$$

While the [Z], [Y] and [S] matrices can be used on a network consisting of an arbitrary number of ports, the transmission (ABCD) matrix is defined for a two-port network by the total voltages and currents as seen on Fig. 2.5.

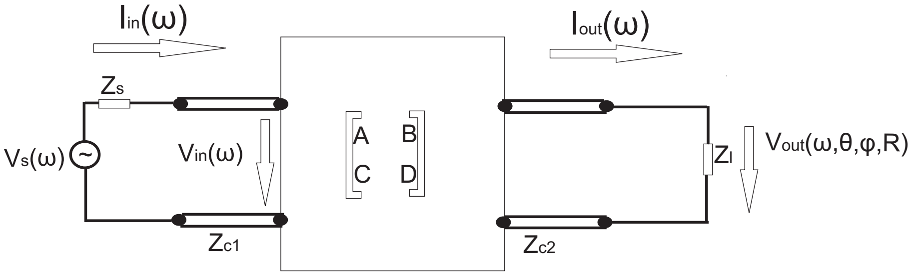

Figure 2.5: The ABCD matrix for a two-port network.

The following equations describes that two-port network:

$$V_1 = AV_2 + BI_2, \tag{2.1.47}$$
$$I_1 = CV_2 + DI_2. \tag{2.1.48}$$

In matrix form, this becomes [38]

$$\begin{pmatrix} V_1 \\ I_1 \end{pmatrix} = \begin{pmatrix} A & B \\ C & D \end{pmatrix} \begin{pmatrix} V_2 \\ I_2 \end{pmatrix}. \tag{2.1.49}$$

2.2 Antennas

The history of antennas starts with James Clerk Maxwell who unified the theories of electricity and magnetism and expressed their relations as a set of equations, known today as Maxwell's Equations. Maxwell published his work in 1874 [47], and he also showed that both light and electromagnetic waves travel as waves with the same speed. Heinrich Rudolph Hertz demonstrated in 1886 the first wireless electromagnetic system. But in was not until 1901 that the first signal was transmitted over a large distance, namely the first transatlantic transmission performed by Gugliemo Marconi. The transmitting antenna consisted of 50 vertically placed wires in the form of a fan. The receiving antenna was a 200 meter long wire pulled by a kite.

Before World War II, most antennas consisted of wires (long wires, dipoles, fans, etc.), and were used as a single element or in arrays. During and after World War II, many other radiators were introduced. This included waveguide apertures, horns, slots and reflectors. The invention of microwave sources (klystron and magnetron) with frequencies of 1 GHz and above is also considered important in the development of antennas. Today, antennas have a wide range of applications, including communication, radar, remote sensing and in the exploration of deep space.

2.2.1 Fundamental parameters of antennas

An antenna *radiation pattern* or *antenna pattern* is a characterization of the electromagnetic field generated by an antenna and can be expressed as a mathematical function or as a graphical representation. The radiation property of most interest is often the two- or three- dimensional spatial distribution of radiated energy as a function of a path or surface of constant radius. A coordinate system with the antenna placed in the origo is shown in Fig. 2.6.

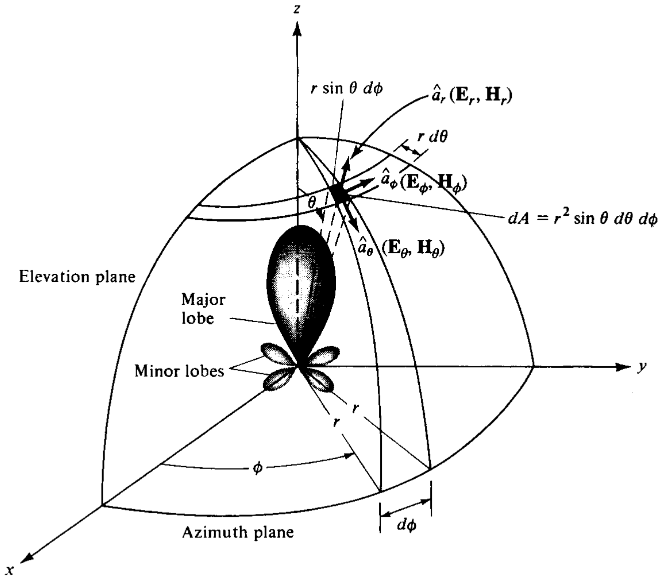

Figure 2.6: Coordinate system for antenna analysis [48].

The received electric or magnetic field at a constant radius is called the amplitude *field pattern*. A graph of the spatial variation of the power density at a constant radius is called an amplitude *power pattern*. These patterns are often normalized with respect to their maximum value. The radiation patterns consist of different parts, often referred to as lobes. These lobes are further divided into the major or main lobe where most of the energy is concentrated and the minor lobes which contains the least energy. A special case of a minor lobe is the back lobe that points in the opposite direction of the main lobe.

Associated with the antenna pattern is a parameter called beamwidth. The beamwidth of a pattern is the angular separation between two identical points located on opposite side of the pattern maximum. The most used beamwidth is the Half-Power Beamwidth (HPBW) that refers to the points where the pattern achieves its half-power, relative to the maximum value. These half-power values are found by setting the value of the field pattern at 0.707 of its maximum and the power pattern at -3 dB (0.5 in a linear scale) value of its maximum.

The space surrounding an antenna is divided into three regions: the reactive near-field, the radiating near-field (Fresnel) and the far-field (Fraunhofer) as seen on Fig. 2.7. The boundaries between these regions are not unique, however, some commonly used criterions exist.

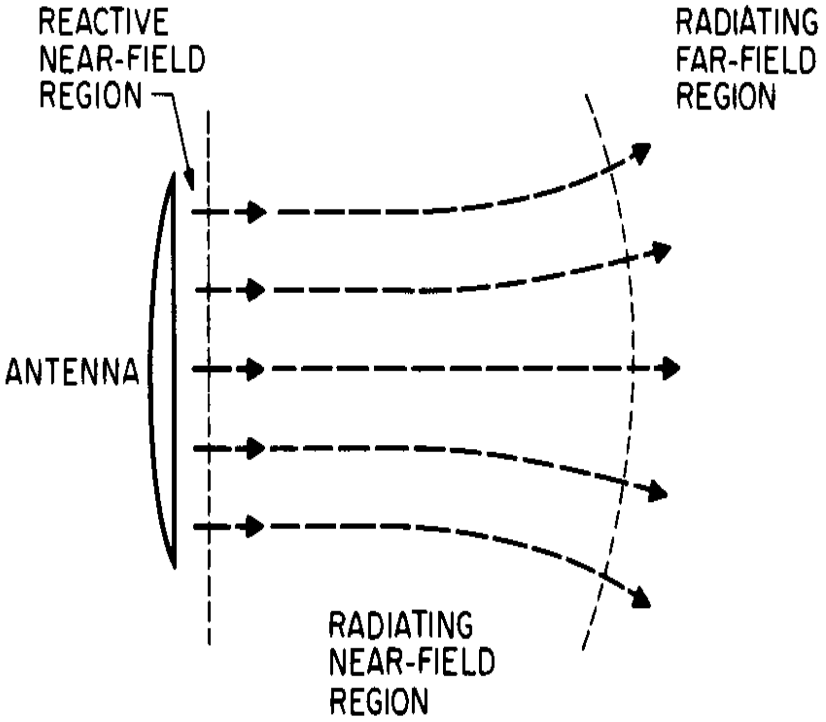

Figure 2.7: The field regions of an antenna [49].

The reactive near-field is defined as

> "That portion of the near-field region immediately surrounding the antenna, wherein the reactive field predominates" [50].

The reactive power is associated with the non-propagating, quasi-static field components which dominate in this region. The reactive component decreases rapidly with the distance from the antenna, and soon it is insignificant compared to the radiating component. The outer boundary of this region is located at a distance $R_1 = 0.62\sqrt{D^3/\lambda}$, where D is the largest dimension of the aperture and λ is the wavelength.

The radiating near-field (Fresnel) region is defined as

> ”That portion of the near-field region of an antenna between the farfield and the reactive portion of the near-field region, wherein the angular field distribution is dependent upon distance from the antenna. If the antenna has a maximum overall dimension that is not large compared to the wavelength, this field region may not exist” [50].

In this region the field pattern is a function of the radial distance and the radial field component can dominate. The outer boundary for the radiating near-field region is taken to be the distance $R_2 = \frac{2D^2}{\lambda}$.

The far-field (Fraunhofer) region is defined as

> ”That region of the field of an antenna where the angular field distribution is essentially independent of the distance from a point in the antenna region” [50].

The field components are mainly transverse (TEM) in this region. There is no outer boundary for the far-field region.

When describing the power associated with an electromagnetic wave, we use the Poynting vector defined as

$$W = E \times H, \tag{2.2.1}$$

where

W=instantaneous Poynting vector (W/m^2).
E=instantaneous electric-field intensity (V/m).
H=instantaneous magnetic-field intensity (A/m).

The total power crossing a closed surface is given by

$$P = \oint\!\!\oint_s W \cdot ds = \oint\!\!\oint_s W \cdot \widehat{\mathbf{n}} ds, \tag{2.2.2}$$

where

P= instantaneous total power (W).
$\widehat{\mathbf{n}}$= unit vector normal to the surface.
da= infinitesimal area of the closed surface (m^2).

Assume time variation on the form $e^{j\omega t}$, where $j = \sqrt{-1}$ and $\omega = 2\pi f$. We can then define the complex electric and magnetic fields $\mathbf{E}$ and $\mathbf{H}$, which can be related to their instantaneous counterparts E and H by the following equations

$$E(x, y, z; t) = Re[\mathbf{E}(x, y, z)e^{j\omega t}], \tag{2.2.3}$$

$$H(x, y, z; t) = Re[\mathbf{H}(x, y, z)e^{j\omega t}]. \tag{2.2.4}$$

By using Eqs. (2.2.3) and (2.2.4), and the identity $Re[\mathbf{E}e^{j\omega t}] = \frac{1}{2}[\mathbf{E}e^{j\omega t} + \mathbf{E}^{*}e^{-j\omega t}]$ where (*) denotes the complex conjugate, the Poynting vector in Eq. (2.2.1) can be written as

$$W = E \times H = \frac{1}{2}Re[\mathbf{E} \times \mathbf{H}^{*}] + \frac{1}{2}Re[\mathbf{E} \times \mathbf{H}^{j2\omega t}]. \tag{2.2.5}$$

This gives us the time average Poynting vector or average power density

$$W_{av}(x, y, z) = [W(x, y, z; t)]_{av} = \frac{1}{2}Re[\mathbf{E} \times \mathbf{H}^{*}]. \tag{2.2.6}$$

Based on Eq. (2.2.6), the average power radiated by an antenna can be written as

$$P_{rad} = \oint_{s}\oint W_{rad} \cdot ds = \oint_{s}\oint W_{av} \cdot \widehat{\mathbf{n}} da = \frac{1}{2}\oint_{s}\oint Re(\mathbf{E} \times \mathbf{H}^{*}) \cdot ds. \tag{2.2.7}$$

Typically, antennas tend to radiate more power in certain directions. This is referred to as the antennas directivity, D, and is defined as follows

> ”The ratio of the radiation intensity in a given direction from the antenna to the radiation intensity averaged over all directions. The average radiation intensity is equal to the total power radiated by the antenna divided by 4π” [50].

In mathematical form

$$D = \frac{U}{U_0} = \frac{4\pi U}{P_{rad}}, \tag{2.2.8}$$

where

D= directivity (dimensionless).

$U = r^2 W_{rad}$= radiation intensity (W/unit solid angle).

U_0= radiation intensity of isotropic source (W/unit solid angle).

P_{rad}= total radiated power (W). Directivity is often expressed in decibels (dB), and the formula for converting the dimensionless quantity to decibels is

$$D(dB) = 10log_{10}[D(dimensionless)] \tag{2.2.9}$$

All antennas suffer from losses caused by reflections due to mismatch between the transmission line and the antenna or from losses in the conducting and dielectric materials. With that in mind, the antenna efficiency can be written as

$$e_0 = e_r e_c e_d \tag{2.2.10}$$

where

e_0= total efficiency (dimensionless).
e_r=$1-|\Gamma|^2$= reflection (mismatch) efficiency (dimensionless).
e_c= conduction efficiency (dimensionless).
e_d= dielectric efficiency (dimensionless).
$|\Gamma|$= reflection coefficient.

It's difficult to calculate e_c and e_d, and Eq. (2.2.10) is therefore often written on the form

$$e_0 = e_r e_{cd} = e_{cd}(1-|\Gamma|^2), \tag{2.2.11}$$

where $e_{cd} = e_c e_d$ is the antenna radiation efficiency, which, as seen later, can be used to relate the gain and the directivity.

Closely related to the directivity, and an often used measure of the antenna performance, is the gain. The antenna gain is defined by IEEE as

> "The ratio of the radiation intensity, in a given direction, to the radiation intensity that would be obtained if the power accepted by the antenna were radiated isotropically. The radiation intensity corresponding to the isotropically radiated power is equal to the power accepted by the antenna divided by 4π" [50].

In mathematical form this is expressed as

$$G = 4\pi \frac{U(\theta,\phi)}{P_{in}}, \tag{2.2.12}$$

where

G= gain (dimensionless).
U= radiation intensity (W/unit solid angle).
P_{in}= power accepted by the antenna (W).

The radiated power can be expressed as $P_{rad} = e_{cd}P_{in}$. Inserting this into Eq. (2.2.12) yields

$$G(\theta,\phi) = e_{cd}\left(\frac{4\pi U(\theta,\phi)}{P_{rad}}\right). \tag{2.2.13}$$

Comparing the right hand side of Eq. (2.2.13) to the directivity given in Eq. (2.2.8), we obtain the following relation between gain and directivity [48]

$$G(\theta,\phi) = e_{cd}D(\theta,\phi). \tag{2.2.14}$$

The phase center of an antenna is the point from which radiation is said to be emitted. This is therefore the spatial reference point of the antenna.

To determine the antenna's phase center as a function of observation angle, the far-field phase properties are considered. The far-field component of the radiated E-vector can be written as

$$E = E(\theta, \phi)F(\theta, \phi) \tag{2.2.15}$$

where $E(\theta, \phi)$ represents the (θ, ϕ) variations of the amplitude and $F(\theta, \phi)$ represents the (θ, ϕ) variations of the phase.

However, this only holds under the assumption that $E(\theta, \phi)$ and $F(\theta, \phi)$ has a $\exp j(\omega t - \beta r)/r$ dependence. If there exists a point in space that reduces the phase function $F(\theta, \phi)$ to a constant, then this point is said to be the phase center of the antenna. The localization of the phase center may also be calculated by finding the point of intersection of successive rays emitted from the antenna, as seen in Fig. 2.8 [51].

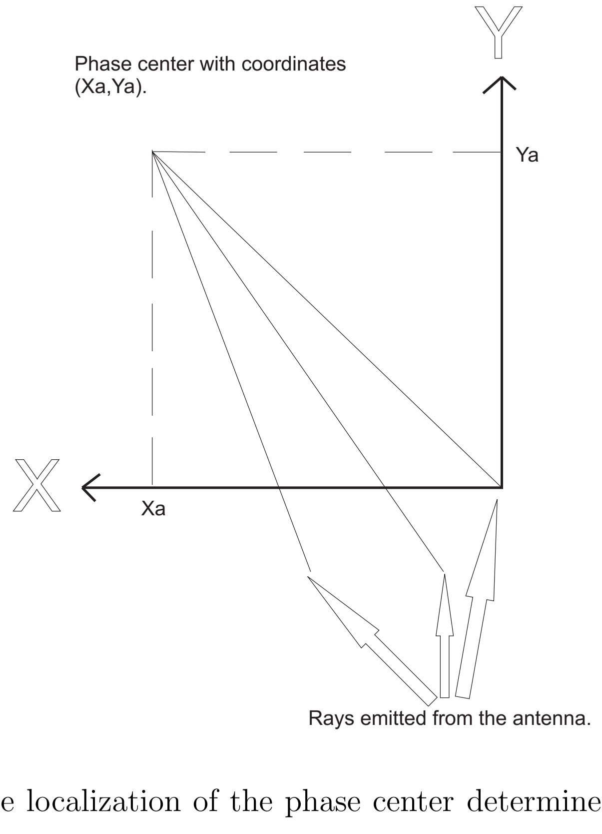

Figure 2.8: The localization of the phase center determined by intersection of rays.

The bandwidth of an antenna is the range of frequencies, on either side of the center frequency, where some antenna characteristics (such as pattern, beamwidth, radiation efficiency and gain) are within an acceptable value compared to the characteristics of the center frequency. For so-called narrowband antennas, the the bandwidth is expressed as a percentage of the frequency difference over the center frequency. For broadband antennas, the bandwidth is expressed as a ratio of the upper-to-lower frequencies of acceptable operation.

Antennas often have an inherent interpropagation time, or a time bias. This means that the signal travels along the antenna before being radiated from some aperture. The time which the signal travels, is referred to as the antenna bias, and can be found by determining the difference between the measured and the theoretical time for the signal to reach a target of known localization.

The initial polarization of a wave is determined by the antenna transmitting the wave. The desired polarization is therefore a factor when designing the antenna. Sometimes, a particular polarization is preferable, in other cases it makes little or no difference. There are three different polarizations; linear, circular and elliptical. A wave is linearly polarized if the electric- or magnetic-field vector is always oriented along the same straight line at a given point in space, as shown in Fig. 2.9. The wave is circularly polarized if the same field vector traces a circle as a function of time. The circular motion can be either clockwise or counterclockwise, seen as the wave travels away from the observer. This also holds for the elliptically polarized wave, where the tip of the field vector traces an elliptical orbit in space [48].

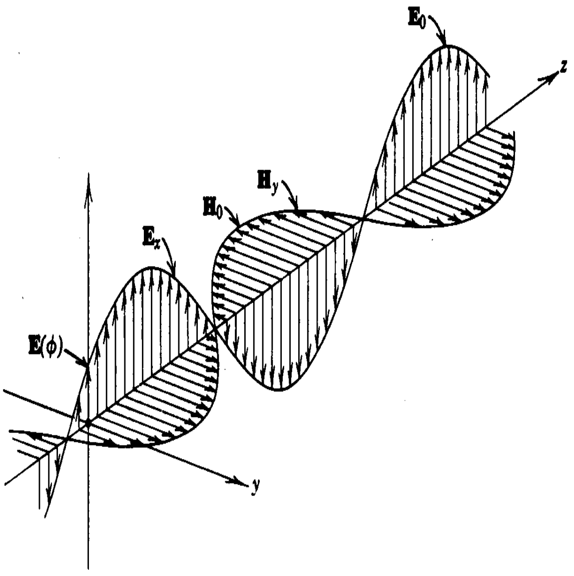

Figure 2.9: The polarization of an electromagnetic wave [52].

2.3 Ultrawideband theory

UWB systems require antennas with a wide operating band, which results in special design and measurement considerations. Therefore, the antenna parameters described in Chapter 2.2.1 does not give a satisfactory characterization of a UWB antenna. New methods have therefore been developed and used to describe the performance of UWB antennas, such as radiation energy pattern, peak amplitude pattern, fidelity, transfer function (impulse response in time domain) and group delay [53]. Some parameters for characterization of the performance of UWB antennas are given below.

The incident signal, $s_1(t)$, of an UWB antenna undergoes a distortion induced by the antenna. This signal distortion can be quantified by first finding the correlation between the incident signal and the radiated one, $s_2(t)$,

$$\int s_1(t)s_2(t-\tau)dt. \tag{2.3.1}$$

The radiated signal can be measured and the fidelity can be found by determining the maximum value of the weighted correlation between $s_1(t)$ and $s_2(t)$:

$$\rho = max_{\tau} \frac{\int s_1(t)s_2(t-\tau)dt}{\left(\sqrt{\int s_1^2(t)\ dt}\right)\left(\sqrt{\int s_2^2(t)\ dt}\right)}, \tag{2.3.2}$$

where τ is the time delay of the signal and $0 \leq \rho \leq 1$. Ideally, this fidelity factor should be as close to 1 as possible, indicating low distortion created by the antenna [54, 55].

The response of an antenna system can be described by the use of transfer functions. As we will see, it is possible to define a transmitting antenna transfer function $\widetilde{\mathbf{H}}_{TA}(\omega, \theta, \varphi)$ (dimensionless), a receiving antenna transfer function $\widetilde{\mathbf{H}}_{RA}(\omega, \theta, \varphi)$ (given in meters) and an antenna system transfer function $H(\omega, \theta, \varphi, R)$ (dimensionless). These transfer functions can be expressed by the ABCD matrix, but it is difficult to measure this parameter and it is therefore easier to apply the S parameters to this two-port network. The functions $\widetilde{\mathbf{H}}_{TA}(\omega, \theta, \varphi)$ and $\widetilde{\mathbf{H}}_{RA}(\omega, \theta, \varphi)$ depend on antenna orientation and operating frequency, and are useful when characterizing pulses from the transmitting antenna or the reflected signal from a target. The antenna system transfer function is more suitable when dealing with UWB communication systems.

Consider an antenna system as shown in Fig. 2.10. The antenna at the left transmits a signal to the antenna on the right, with a distance R between them. The transmitting antenna transfer function is defined by the ratio of

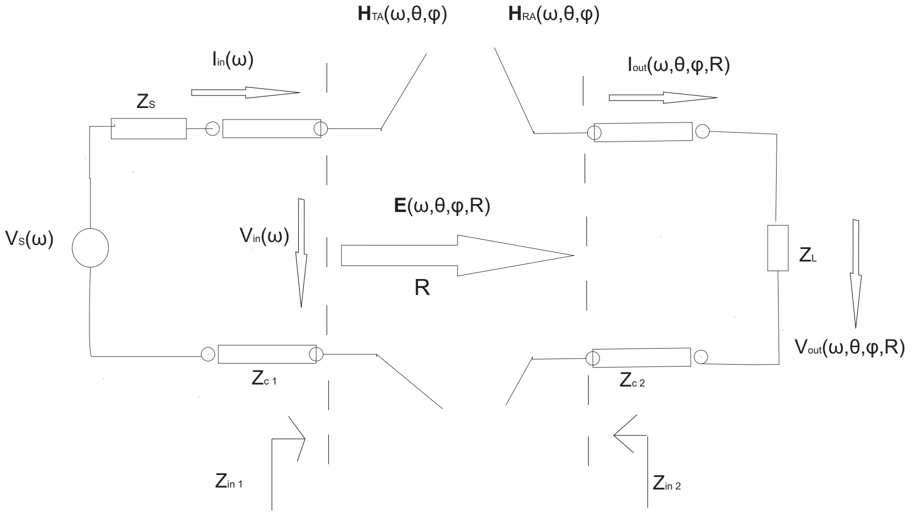

Figure 2.10: Transmitting and receiving antenna circuits used in the derivation of the transfer functions.

the distance normalized electric far-field, $\mathbf{E}(\omega,\theta,\varphi) = \mathbf{E}(\omega,\theta,\varphi,R)/\frac{e^{-jkR}}{R}$ at a given point in space to the input signal of the transmitting antenna

$$\begin{aligned} \widetilde{\boldsymbol{H}}_{TA}(\omega,\theta,\varphi) &= H_{TA}(\omega,\theta,\varphi)\boldsymbol{\rho}_{TA} \\ &= \frac{\boldsymbol{E}(\omega,\theta,\varphi)}{V_{in}(\omega)} \\ &= \frac{\boldsymbol{E}(\omega,\theta,\varphi,R)}{V_{in}(\omega)} Re^{jkR}. \end{aligned} \tag{2.3.3}$$

In a similar way, the receiving antenna transfer function can be defined as the ratio of the output signal of the receiving antenna to the incident electric field

$$\widetilde{\boldsymbol{H}}_{RA}(\omega,\theta,\varphi) = H_{RA}(\omega,\theta,\varphi)\boldsymbol{\rho}_{RA} = \frac{V_{out}(\omega,\theta,\varphi,R)}{\boldsymbol{E}(\omega,\theta,\varphi,R)}. \tag{2.3.4}$$

The definition of the antenna system transfer function is the ratio of the output signal to the exciting signal

$$H(\omega,\theta,\varphi,R) = \frac{V_{out}(\omega,\theta,\varphi,R)}{V_s(\omega)}. \tag{2.3.5}$$

In these equations $\omega = 2\pi f$, f is the operating frequency, k is the wavenumber in free space, ρ_{TA} and ρ_{RA} are unit vectors of the polarization direction for the transmitting and receiving antennas, respectively. If the impedances defined in Fig. 2.10 have the relation $Z_s = Z_{c1} = Z_{c2} = Z_l$ and assuming

$|\rho_{TA} \cdot \rho_{RA}| = 1$, the transfer functions can be expressed by the S parameters as

$$H_{TA}(\omega, \theta, \varphi) = \sqrt{\frac{2S_{21}}{(1+S_{11})(1-S_{22})} \frac{j\omega}{2\pi c} Re^{jkR}}, \tag{2.3.6}$$

$$H_{RA}(\omega, \theta, \varphi) = \sqrt{\frac{2S_{21}}{(1+S_{11})(1-S_{22})} \frac{2\pi c}{j\omega} Re^{jkR}}, \tag{2.3.7}$$

$$H(\omega, \theta, \varphi, R) = \frac{S_{21}}{2}. \tag{2.3.8}$$

where

c is the speed of light in vacuum.

The transfer functions are preferably measured in the frequency domain by the use of a network analyzer because of the high accuracy in these measurements. It is also possible to obtain these functions from the time domain by taking the Fourier transform of the impulse response [53].

A UWB antenna can also be seen as a filter with both magnitude and phase response. Given a filter response $H(f) = A(\omega)e^{j\theta(\omega)}$, the group time delay is defined as the negative derivative of the filter phase with respect to frequency

$$\tau_g = -\frac{d\theta(\omega)}{d\omega}. \tag{2.3.9}$$

There are two aspects of the group time delay that we need to address, namely magnitude and phase. The magnitude of the group time delay directly affect the magnitude of the system or network signal and can lead to a damping effect. The group time delay is also closely related to the signal propagation distortion. This means that the output waveform may undergo some distortion. It is important to be aware of that these two aspects are independent of each other, and that the group time delay alone does not give a complete answer to which of these two effects that actually occur [56, 57].

2.4 Beamforming

Beamforming is a technique used to control the directivity or sensitivity of an array of antenna transmitters or receivers. When receiving a signal, beamforming can increase the receiver sensitivity with regard to the wanted signals and decrease the sensitivity of interference and noise. When transmitting a signal, beamforming can increase the power in the direction the signal is to be sent.

The beamforming technique, used in our simulations, was the delay-and-sum beamforming. This technique gives the transmitted signals y(t) an appropriate delay Δ, so that the waves reach the target at the same time, and are summed together. If a scattering object exists in the focal point, the signals will add coherently and give a larger power result than elsewhere. Systematically changing the focal point throughout the entire area of interest, a microwave map of the region can be created and significant scattering points can be detected and localized. This beamforming technique can be used as a part of the post-processing of the signals (assuming that the signals from each antenna in the array are transmitted simultaneously) or as an active beamforming by giving the signals an appropriate delay *before* they are transmitted. A schematic diagram of the delay-and-sum beamforming is shown in Fig. 2.11.

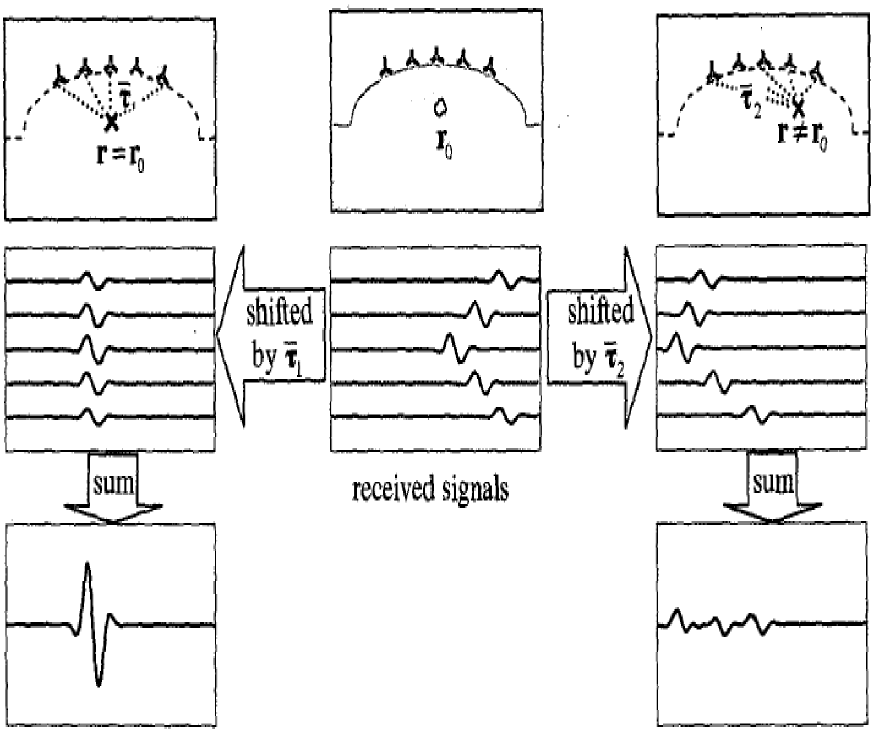

Figure 2.11: The delay-and-sum beamforming, with the received signals in the middle. When the beamformer has the right time shifts, the signals add coherently as show on the left, and on the right side the incoherent summation is shown when the time shifts are incorrect [17].

It was the active beamforming technique that was used in this project. But, in order to get the best result possible, the beamforming must take into consideration both phase and amplitude when focusing the signals. Therefore, it is necessary to know both the time delay and the amplitude at the scattering point. In this way, every antenna contributes in an equal amount and an optimal result can be obtained. The time delay of each of the antennas can be found by first establishing the theoretical distance from the antenna to the target. These distances can be converted to time by using the following equation, which is dependent of the media that the signal propagates into:

$$s = vt \Rightarrow t = \frac{s}{v} = \frac{s}{c/\sqrt{\epsilon}}, \tag{2.4.1}$$

where c is the speed of light in vacuum and ϵ is the dielectric constant of the medium in which the signal propagates. The antenna signal with the longest propagation distance to the target has to be transmitted first, and is used as a reference for the other antennas. The reference antenna is given a time delay of 0 ns. The time delays for the other antennas are found by calculating the difference between the time parameter, found in Eq. (2.4.1), for the reference antenna and each of the other antennas. The amplitude that the transmitting signals must have in order to contribute equally at the target, can be found by measuring the electric field at the center of the scattering point and calculating the signal amplitudes by the following formula

$$P_{signal} = \sqrt{P_x^2 + P_y^2 + P_z^2} \tag{2.4.2}$$

where P_x^2, P_x^2 and P_x^2 are the maximum signal amplitude measured in the x-, y- and z-direction. The antenna signal with the largest amplitude in this point is given the transmitting amplitude 1. The amplitudes of the other antenna signals are raised accordingly, so that all signals contribute in an equal amount.

2.5 The simulation method

CST Microwave Studio is a electromagnetic simulator based on the Finite Integration Technique (FIT), which was first proposed by Weiland in 1976 [58]. A short introduction to this simulation method will be given, along with a short description of the different solvers available.

2.5.1 The Finite Integration Technique

FIT discretizes the following integral form of Maxwell's equations:

$$\oint_{\partial A} \vec{E} \cdot d\vec{s} = -\int_A \frac{\partial \vec{B}}{\partial t} \cdot d\vec{A} \tag{2.5.1a}$$

$$\oint_{\partial A} \vec{H} \cdot d\vec{s} = \int_A \left(\frac{\partial \vec{D}}{\partial t} + \vec{J} \right) \cdot d\vec{t} \tag{2.5.1b}$$

$$\oint_{\partial V} \vec{D} \cdot d\vec{A} = \int_V \rho \cdot dV \tag{2.5.1c}$$

$$\oint_{\partial V} \vec{B} \cdot d\vec{A} = 0 \tag{2.5.1d}$$

where

$\vec{E}$ is the electric field.

$\vec{H}$ is the magnetic field.

$\vec{B}$ is the magnetic flux density.

$\vec{D}$ is the electric displacement field.

$\vec{J}$ is the free current density.

ρ is the free electric charge density.

In order to solve these equations, a finite calculation domain that encloses the considered problem is defined. The problem is split up into small cuboids, also called grid cells. These grid cells form a mesh system: the primary grid G and the dual grid $\tilde{G}$, which is set up orthogonally to the first one. As seen in Fig. 2.12, the electric grid voltages $\vec{e}$ and magnetic fluxes $\vec{b}$ are allocated on the primary grid, while the dielectric edge fluxes $\vec{d}$ and the magnetic grid voltages $\vec{h}$ are on the dual grid.

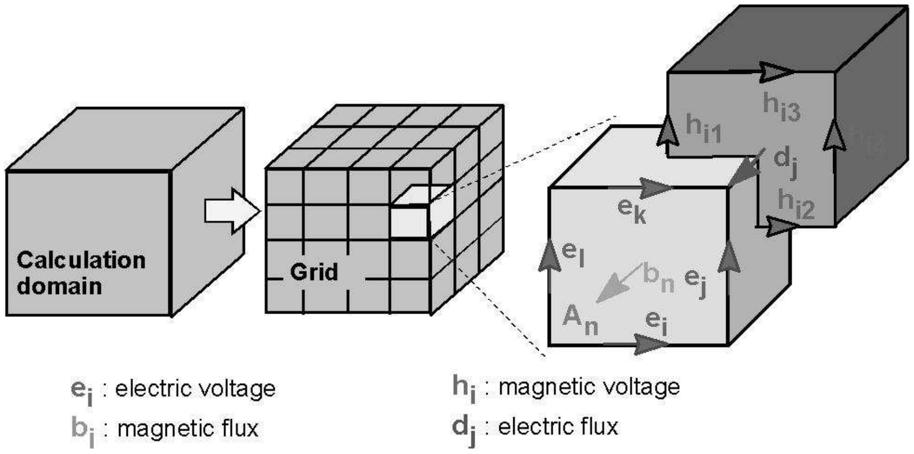

Figure 2.12: The electric grid voltages and magnetic fluxes are allocated on the primary grid, while the dielectric facet fluxes and the magnetic grid voltages are on the dual grid [59].

Considering Faraday's law, each cell has a closed integral on the equations left-hand side that can be written as a sum of four grid voltages. Because of this, the time derivative of the magnetic flux defined on the enclosed primary cell edge represents the right-hand side of the equation. By repeating this procedure for all cell borders, the calculation rule can be summarized in a matrix formulation, where the matrix C is introduced as the discrete equivalent of the curl operator. By applying Ampere's law on the dual grid, the discrete curl operator $\tilde{C}$ is introduced. Similarly, the discrete divergence operator S and $\tilde{S}$ are defined. The complete discretized set of Maxwell's grid equations (MGE) are thereby obtained:

$$\underline{Ce} = -\frac{d}{dt}\underline{b} \tag{2.5.2a}$$

$$\underline{\tilde{C}h} = \frac{d}{dt}\underline{d} + \underline{J} \tag{2.5.2b}$$

$$\underline{\tilde{S}d} = \underline{q} \tag{2.5.2c}$$

$$\underline{Sb} = \underline{0} \tag{2.5.2d}$$

No additional error has been introduced at this point. This is essential in FIT discretization and is reflected by the fact that the properties of the continuous gradient, curl and divergence are still valid in grid space:

$$div\ rot \equiv 0 \leftrightarrow \underline{SC} = \underline{\tilde{S}\tilde{C}} = \underline{0} \tag{2.5.3}$$

$$rot\ grad \equiv 0 \leftrightarrow \underline{C\tilde{S}^T} = \underline{\tilde{C}S^T} = \underline{0} \tag{2.5.4}$$

Finally, the material equations introduce the inevitable numerical inaccuracy due to the spatial discretization:

$$\underline{d} = \underline{M_\epsilon e} \tag{2.5.5}$$

$$\underline{b} = \underline{M_\mu h} \tag{2.5.6}$$

$$\underline{j} = \underline{M_\sigma e} + \underline{j}_s \tag{2.5.7}$$

Now, all matrix equations are available to solve electromagnetic field problems on the discrete grid space [59, 60].

2.5.2 The CST Microwave Studio solvers

There are three different solvers available when solving high frequency electromagnetic field problems: transient, frequency and eigenmode solver.

- Transient Solver
  The CST Microwave Studio transient solver allows the simulation of a problem in a wide frequency range in one single computation run. This is therefore an efficient solver for problems containing nonzero sources, open boundaries or devices with large dimensions.

- Frequency Domain Solver
  The CST Microwave Studio frequency solver is based on Maxwell's equations in the harmonic case where $\partial/\partial t \rightarrow i\omega$. This solver is useful when dealing with small-size problems and only a few frequency points are needed for solving the problem.

- Eigenmode Solver
  The CST Microwave Studio eigenmode solver is best suitable for solving problems regarding closed structures. This solver calculates the structure's eigenmodes and corresponding eigenvalues [60].

2.6 Simulation setup

The simulations were done with CST Microwave Studio, described in chapter 2.5, and the results were imported and post-processed in Matlab. The substrate of the antenna was a dielectric material with $\epsilon = 3.36$ and $\mu = 1$. The thickness of the substrate was 1.01 mm. Two ellipses were carved out on the top of this substrate. A lossy biological load was also implemented and fat was used as a load with $\epsilon = 10$, $\mu = 1$ and an electrical conductivity of σ=0.4. The thickness of the fat was 100 mm. All simulations were done by using this setup as a starting point and is seen on Fig. 2.13(a). A sideview of the antenna is seen on Fig. 2.13(b). Several different versions of this model were tested. The sizes of the two ellipses were changed in order to find the optimal antenna behavior, the same held for changing the value of the resistance. After finding an optimal working antenna, this design was kept throughout the rest of the simulations.

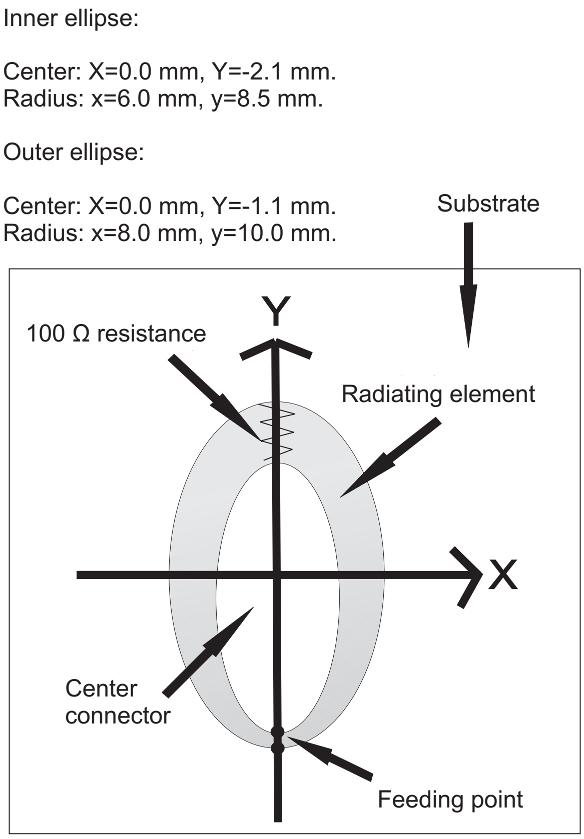

Inner ellipse:

Center: X=0.0 mm, Y=-2.1 mm.
Radius: x=6.0 mm, y=8.5 mm.

Outer ellipse:

Center: X=0.0 mm, Y=-1.1 mm.
Radius: x=8.0 mm, y=10.0 mm.

(a) The front of the antenna.

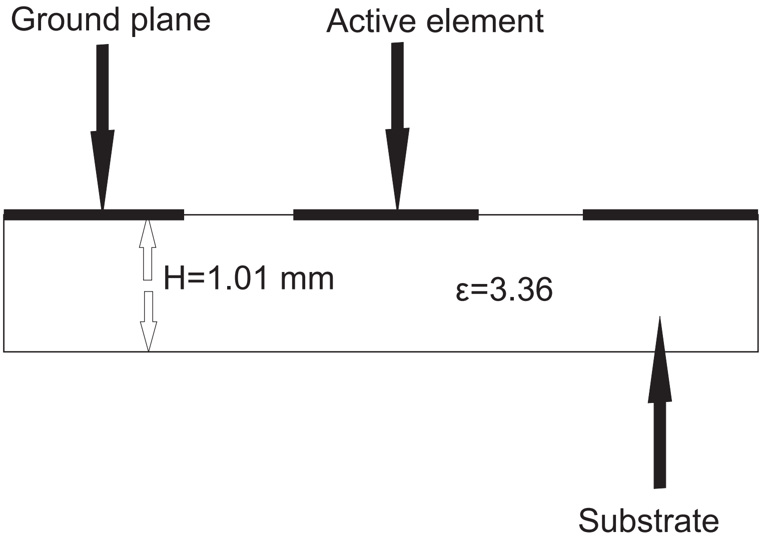

(b) A sideview of the antenna.

Figure 2.13: Drawings showing the geometry of the antenna seen from the front and side.

To test the antennas, a scattering target was placed inside the fat, one-by-one, in a pattern as shown in Fig. 2.14. First, a solid spherical perfectly electrical (PEC) material was used. the sphere was given a diameter of 4.0 mm. Later, the material was changed to cancerous tissue with the dielectrical properties $\epsilon = 50$, $\mu = 1$ and an $\sigma = 1.4$. The antenna then tried to identify the returned signal and based on that, give an estimate of the distance from the antenna to the tumor.

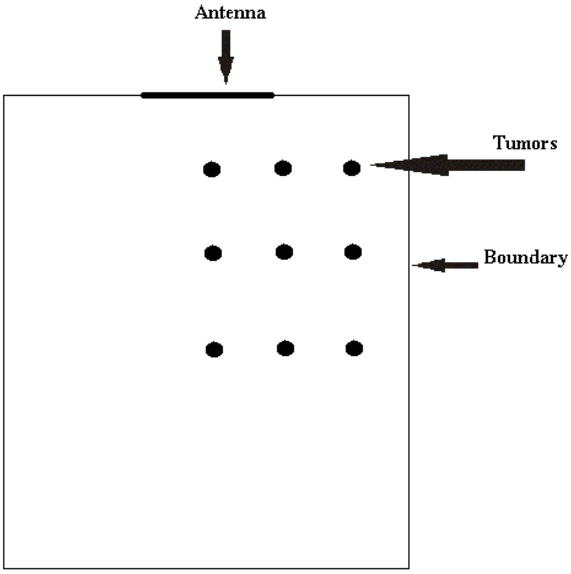

Figure 2.14: A schematic showing the antenna and the position of nine different tumors, seen from above.

The setup was later expanded to include four antennas surrounding the fat which contained a scattering target consisting of cancerous tissue. This setup can be seen on Fig. 2.15, which allows us to see the three different target localizations used. In all of these cases, the target was placed in the y=0 plane and the position of the tumor was always estimated on the basis of the x- and z-coordinates.

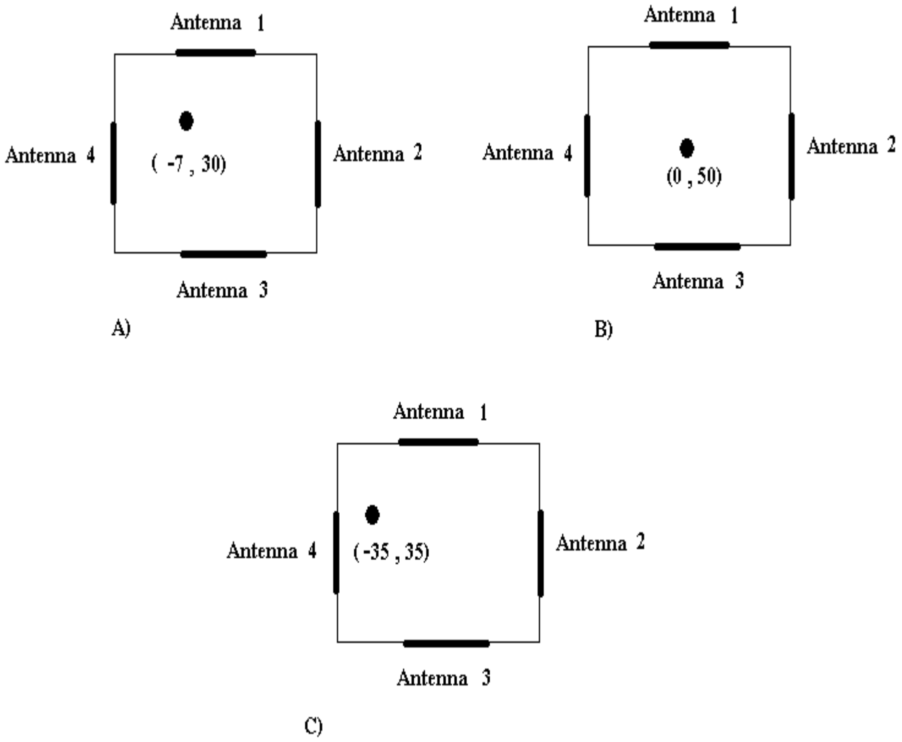

Figure 2.15: A schematic (seen from above) showing the different setup used in the model consisting of four antennas and a tumor. The tumor is placed in three different locations; a) (-7 , 30) b) (0 , 50) c) (-35 , 35).

Chapter 3

Results

3.1 Antenna characteristics

The lumped element resistance of the antenna was varied from 50 Ω to 200 Ω in steps of 50 Ω, and the lumped element of 100 Ω, along with the geometry in Fig. 2.13(a), gave the best S_{11}-parameter. A graph of the S_{11}-parameter over the frequency range 1 GHz to 11 GHz can be seen in Fig. 3.1, where the maximum value is -12.19 dB.

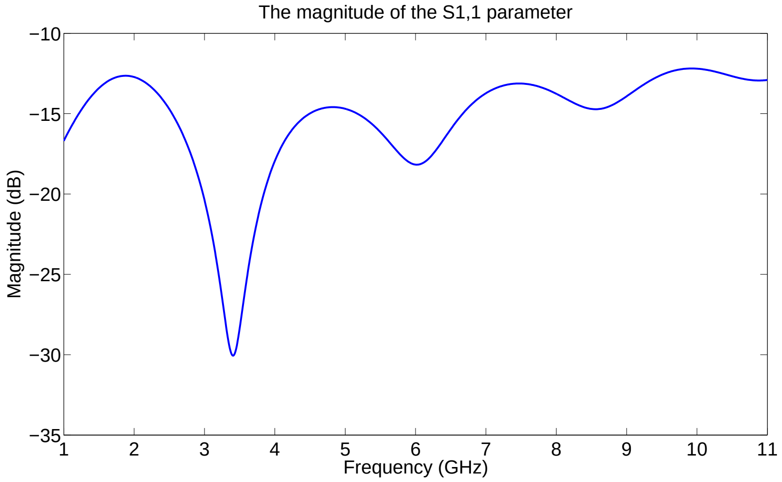

Figure 3.1: A graph of the S_{11}-parameter found when using the antenna shown in Fig. 2.13.

The transmitted signal, represented in both the time- and frequency domain, can bee seen in Fig. 3.2. In CST Microwave Studio, the transmitted pulse was set to range from 1 GHz to 11 GHz. These frequencies are marked by dashed lines in Fig. 3.2(b). The amplitude of these frequency components can be compared to the maximum value, usually measured at the center frequency. The 1 GHz component was found to be 10.0% of the maximum value, while the 11 GHz component was 10.3%.

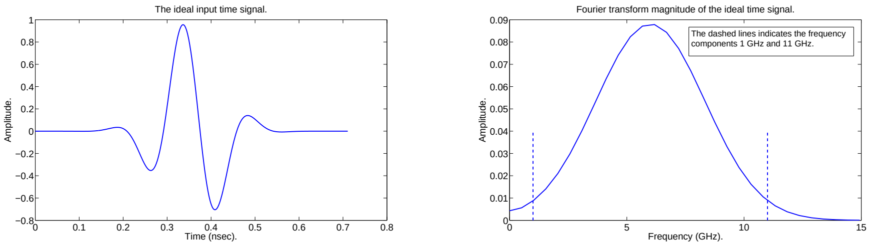

(a) The transmitted signal in the time domain.

(b) The transmitted signal in the frequency domain.

Figure 3.2: The transmitted signal.

After establishing the transmitted signal, this signal was transmitted through an antenna and into a lossy biological load. The electric field waveforms as a function of observation angle in the horizontal and vertical direction at a constant distance of 50 mm from the antenna was obtained and is presented in Figs. 3.3 and 3.4.

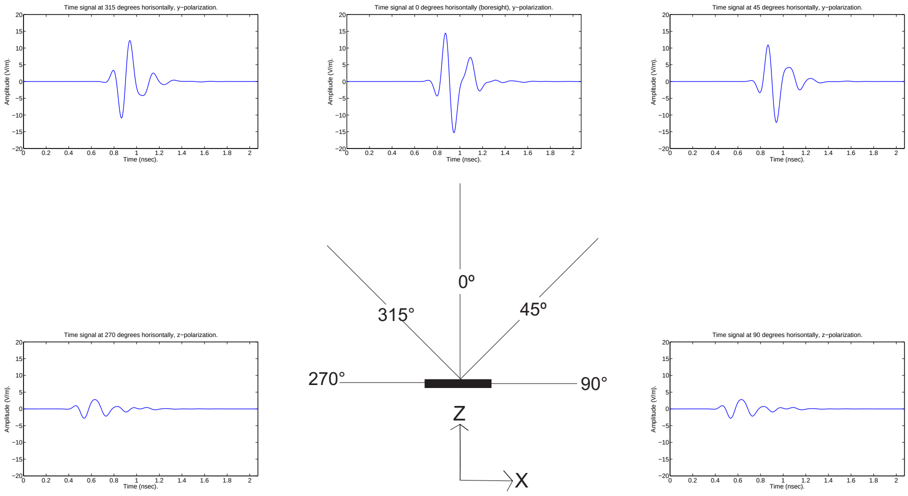

Figure 3.3: E-plane waveforms as a function of observation angle in the horizontal y=0 plane.

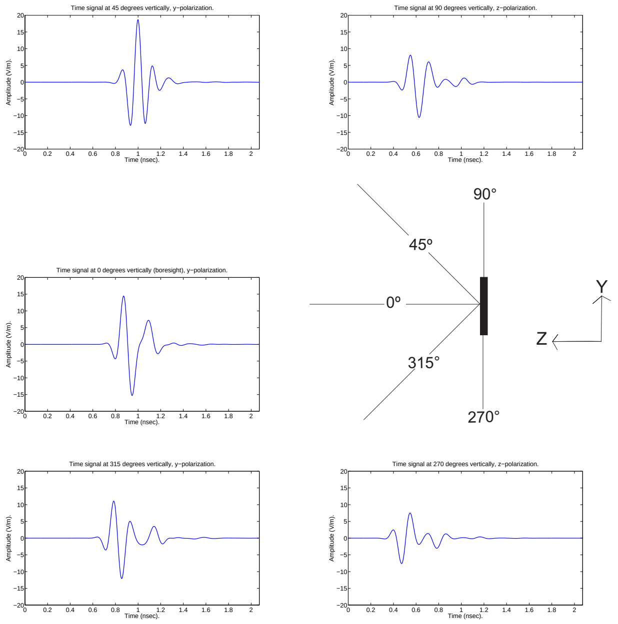

Figure 3.4: E-plane waveforms as a function of observation angle in the vertical x=0 plane.

Virtual probes measuring the electric field were placed in a regularly pattern at a distance z=5 mm, z=10 mm and z=20 mm from the antenna. Probes were not placed at negative x-values because of symmetry. The time signals from these probes were post-processed and the fidelity factor was calculated by the use of Eq. (2.3.2). Contour plots of the fidelity are shown in Figures 3.5 - 3.7. The maximum and minimum fidelity found, was 0.99 and 0.63 respectively. The mean fidelity of the contributing probes was found to be 0.8629.

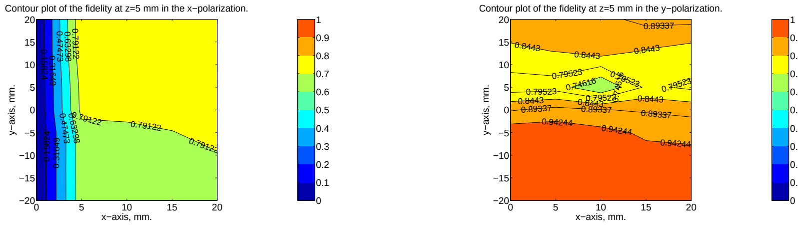

(a) The x polarization. (b) The y polarization.

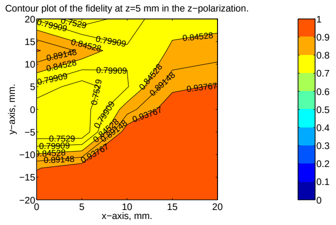

(c) The z polarization.

Figure 3.5: Contour plot of the fidelity at a distance of 5 mm from the antenna.

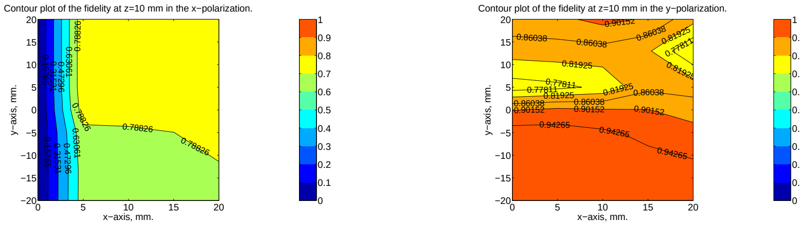

(a) The x polarization. (b) The y polarization.

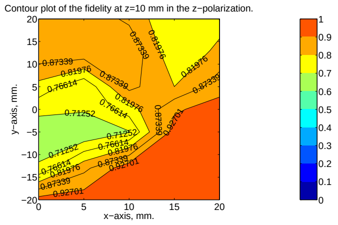

(c) The z polarization.

Figure 3.6: Contour plot of the fidelity at a distance of 10 mm from the antenna.

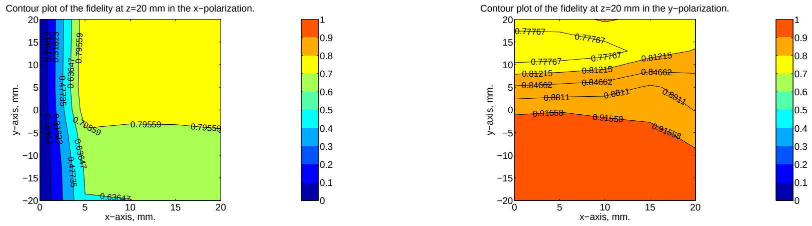

(a) The x polarization.
(b) The y polarization.

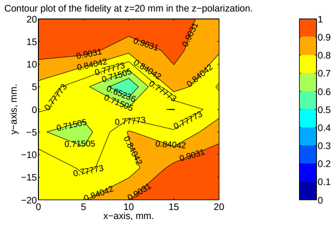

(c) The z polarization.

Figure 3.7: Contour plot of the fidelity at a distance of 20 mm from the antenna.

The antenna group time delay, described on page 28, was found between antenna 1 and 3 with locations as seen in Fig. 2.15 and can be seen in Fig. 3.8. The deviation in group time delay over the entire frequency range was 3.7215 nanoseconds, with a mean value of 1.468 nanoseconds. The magnitude and phase of the S-parameter between these two antennas is shown in Fig. 3.9.

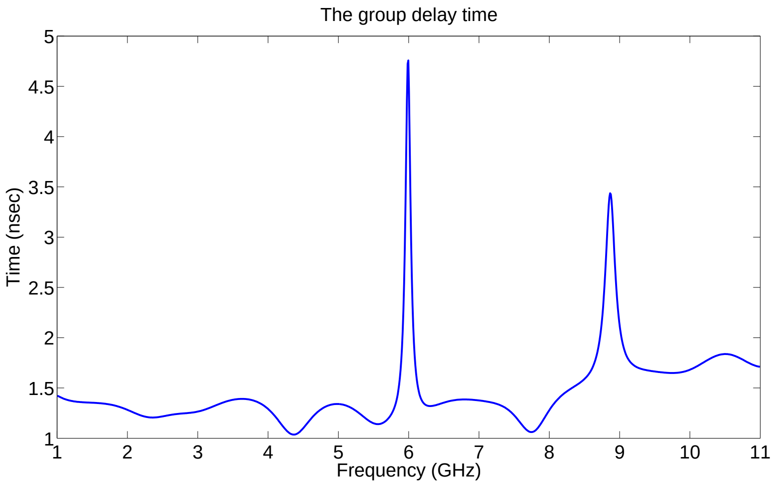

Figure 3.8: Plot of the group time delay found between antenna number 1 and 3 on Fig. 2.15.

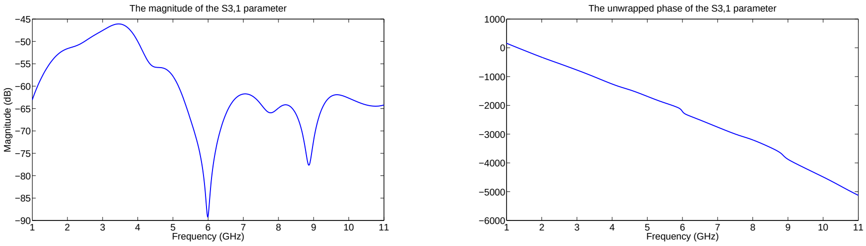

(a) The magnitude of the S_{31}-parameter.

(b) The unwrapped phase of the S_{31}-parameter, exported from CST Microwave Studio.

Figure 3.9: Plot of the magnitude and phase of the S_{31}-parameter found between antenna number 1 and 3 on Fig. 2.15.

Another antenna parameter that was important to establish, was the antenna interpropagation time. The antenna interpropagation time was found by using the approach described on page 25. The average antenna interpropagation time was 0.10967 nsec.

By using CST Microwave Studio, the electric field could be measured at the planes z=10 mm and z=20 mm for the frequencies 1, 3, 5, 7, 9 and 11 GHz to visualize the radiation pattern exhibited by the antenna. These datas were post-processed and are displayed graphically as contour plots of the x- , y- and z- polarizations together with the total electric field at each frequency. These plots also include the -3dB and -6dB contour levels. The contour plot of the radiation pattern found at the z=10 mm plane and at a frequency of 1 GHz is shown below in Fig. 3.10. The rest of the plots are listed in Appendix A. The -3dB width of all these graphs are listed in Tables 3.1 and 3.2. When multiple -3dB contours occur, the widest one is listed. From the calculations of the radiation patterns, the maximum values from the different polarizations and frequencies was extracted. These values are listed in Tables 3.3 and 3.4.

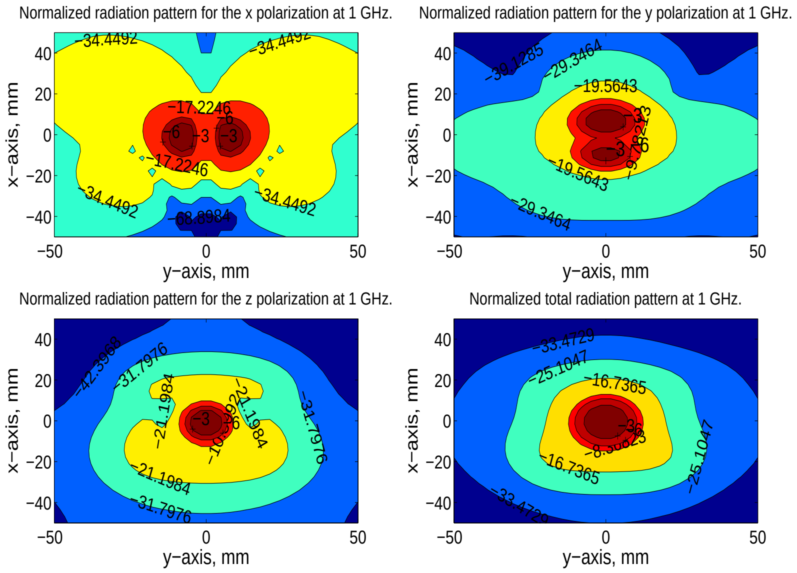

Figure 3.10: Radiation pattern measured at the plane z=10mm and at a frequency of 1 GHz. Values are given in dB.

Frequency (GHz)	E_X	E_Y	E_Z	E_{total}
1	8	13	10	14
3	11	16	10	18
5	9	12	8	19
7	8	18	7	17
9	7	20	7	15
11	6	26	5	22

Table 3.1: -3dB width (in mm) of the x-,y-,z-polarization and the total radiation pattern, all measured at z=10 mm from the antenna.

Frequency (GHz)	E_X	E_Y	E_Z	E_{total}
1	14	24	15	22
3	17	24	16	30
5	18	19	12	31
7	15	16	10	26
9	10	30	11	24
11	10	36	10	24

Table 3.2: -3dB width (in mm) of the x-,y-,z-polarization and the total radiation pattern, all measured at z=20 mm from the antenna.

Frequency (GHz)	x polarization	y polarization	z polarization	Total
1	87.27	96.33	169.03	178.80
3	110.70	205.00	159.20	238.00
5	176.89	203.98	176.34	275.94
7	207.68	214.21	202.52	307.52
9	219.98	210.85	218.29	320.03
11	226.12	198.67	223.63	300.90

Table 3.3: Maximum power values of the different polarizations measured at given frequencies and at a distance of 10 mm from the antenna.

Frequency (GHz)	x polarization	y polarization	z polarization	Total
1	18.16	27.56	37.83	46.35
3	45.88	112.61	50.62	116.24
5	75.17	119.74	68.85	132.39
7	94.72	116.27	92.85	146.33
9	105.57	113.88	93.08	141.57
11	106.62	100.74	96.98	141.10

Table 3.4: Maximum power values of the different polarizations measured at given frequencies and at a distance of 20 mm from the antenna.

When trying to establish the phase center of the antenna, probes were placed at the following x- and y- coordinates: x=0,10,20,30,40 mm and y=-40,-30,-20,-10,0,10,20,30,40 mm. This pattern was repeated for the following z-coordinates: z=5,15,25,35,45 and 55 mm. This gives a total of 270 observation points. The distance from the antenna to these points in space were estimated and the average interpropagation time found earlier was taken into account. The estimated distance was compared to the theoretical one, which used the center of origin as a reference point. Tables 3.5 and 3.6 gives a description of the deviation from origo for the x- and y-coordinates respectively, assuming that the phase center is located on the antenna, i.e. on the z=0 mm plane. With respect to the x-coordinates, 76.3% of the observations are within ±10 mm of the origo. In the case of the y-coordinates, 75.9% of the observations are within -10 mm of the origo. Based on these comparisons between the true and the estimated distances, an area containing the phase center was determined and is shown in Fig. 3.11.

Deviation intervals	Number of observations	% of total observations
0 mm → $\vert 5\vert$ mm	133	49.3%
$\vert 5\vert$ mm → $\vert 10\vert$ mm	73	27%
$\vert 10\vert$ mm ≥	64	23.7%

Table 3.5: Deviation of the x-coordinate from the origo for establishing a phase center.

Deviation intervals	Number of observations	% of total observations
0 mm → $\vert 5\vert$ mm	131	48.5%
$\vert 5\vert$ mm → $\vert 10\vert$ mm	74	27.4%
$\vert 10\vert$ mm ≥	65	24.1%

Table 3.6: Deviation of the y-coordinate from the origo for establishing a phase center.

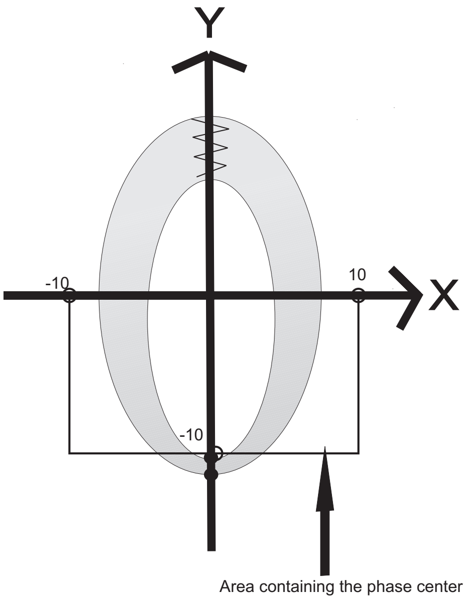

Figure 3.11: The antenna and the area containing the phase center.

After finding the interpropagation time and the phase center, the model was expanded to also include a tumor with the dielectric properties described in Chapter 2.6. This tumor was placed at different distances and angles from the antenna, as seen on Fig. 2.14. Post processing was performed on the signals in order to recognize the scattered signal from the tumor and thereby estimating the distance from the antenna to the tumor. These results can be seen in Table 3.7. It is seen that the largest deviation in the estimation of distance is 3.9 mm, which constitutes 15.6 % of the exact distance. It is important to be aware of, that when discussing the true distance from an antenna to the tumor, we mean the distance from origo of the local antenna coordinate system, shown in Fig. 2.13(a), to the center of the tumor.

Tumor Coordinates (mm)	True Distance (mm)	Estimated Distance (mm)	Deviation (%)
(0 , 15)	15.0	13.6	9.3
(20 , 15)	25.0	21.1	15.6
(40 , 15)	42.7	40.4	5.4
(0 , 35)	35.0	34.9	0.3
(20 , 35)	40.3	40.3	0.0
(40 , 35)	53.2	52.5	1.3
(0 , 55)	55.0	57.0	3.6
(20 , 55)	58.5	58.0	0.9
(40 , 55)	68.0	68.3	0.4

Table 3.7: The coordinates of the tumors, the true and estimated distance from the antenna to the tumors.

3.2 Antenna beamforming

The previous model was further expanded to include four identical antennas and a tumor. The position of the antennas relative to the tumor at (0, 50) are shown in Fig. 2.15(b). First, the four antennas transmitted their signal in a successive matter and received the scattered signal independently of each other. 1/2 of the voltage was transmitted, noise was added to the signals coming from each of the four channels and the delay-and-sum beamforming was applied as a part of the signal post-processing. 2D and 3D plots showing the localization of the tumor with a noise level of $1.0 \cdot 10^{-7}$ added, is seen on Figs. 3.12(a) and 3.12(b). Then, active beamforming on the transmitter was applied in addition to the post-processing previously mentioned. Since all antennas have the same distance to the tumor, there was no delay between the different channels and the amplitudes were also the same, namely 1. All antennas transmitted their signal at the same time and the result are seen on Fig. 3.12(c).

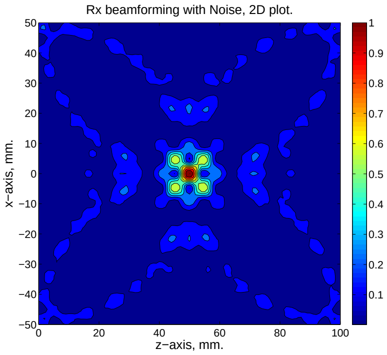

(a) 2D plot for estimating the localization of a tumor at (0 , 50) with Rx beamforming. The estimated position of the tumor is (0 , 50).

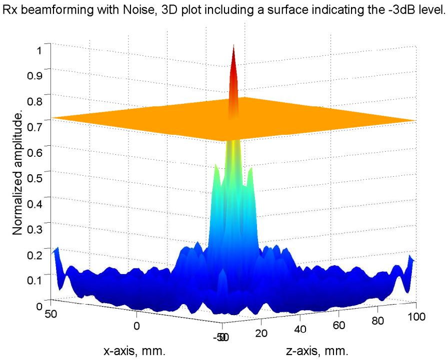

(b) A 3D view of the same area as in (a) including a surface showing the -3dB level.

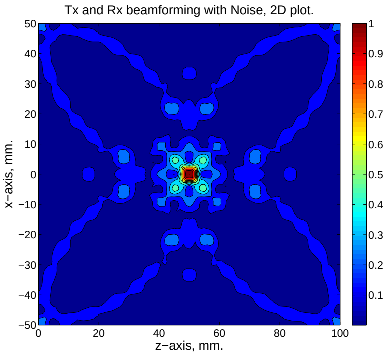

(c) 2D plot for estimating the localization of a tumor at (0 , 50) with both Tx and Rx beamforming. The estimated position of the tumor is (0 , 50).

Figure 3.12: Maps showing the localization of a tumor at (0 , 50) and a noise level of $1.0 \cdot 10^{-7}$ added to the signals.

The noise level was increased in both cases until the system no longer could determine the true localization of the tumor. The signal-to-clutter ratios as a function of the noise added can be seen on Fig. 3.13. The SNR and (S/C) ratios to these noise levels are documented in Tables B.1 and B.2. Since the calculation of the signal-to-clutter ratios were depending on a scaled random variable, namely the added noise, these calculations were averaged over 100 runs to secure an accurate result.

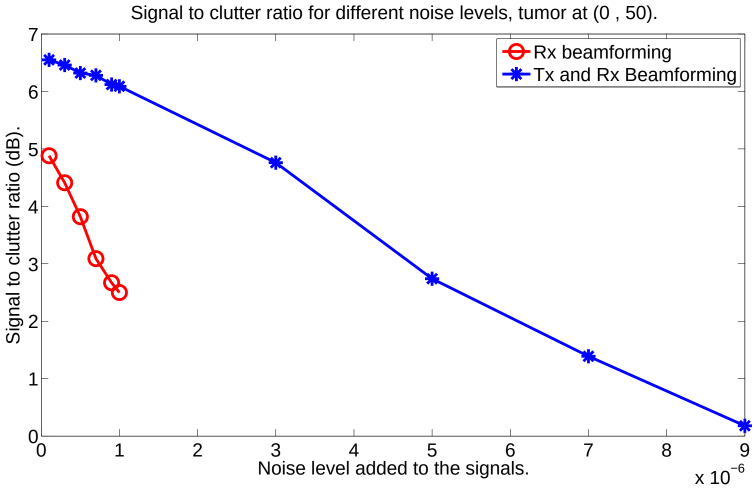

Figure 3.13: The signal-to-clutter ratios when adding different noise levels to the signals and the tumor placed at (0 , 50).

In the next model, the tumor was placed in (-7 , 30) as shown on Fig. 2.15(a). The transmitting and receiving method from the previous model was repeated for the case of Rx beamforming. When applying Tx-Rx beamforming, the signals had to be transmitted in a specific order, and with a given time delay, to arrive at the tumor simultaneously. This time delay was found as described in Chapter 2.4. When the distance to the tumor is different for each of the four antennas, there is a second way to perform beamforming at the transmitter, namely to correct for both the time delay and the amplitude so that the signals arrive at the tumor simultaneously and contribute in an equal amount. The time delays for the antennas, the corrected amplitudes and the transmitting sequences are given in Table C.1.

Plots showing the localization of the tumor at (-7 , 30) with a noise level of $1.0 \cdot 10^{-7}$ added, are seen on Fig. 3.14. The signal-to-clutter ratios as a function of the noise added, are found in Fig. 3.15. Tables B.3 - B.5 lists the corresponding noise levels, SNR and S/C ratios.

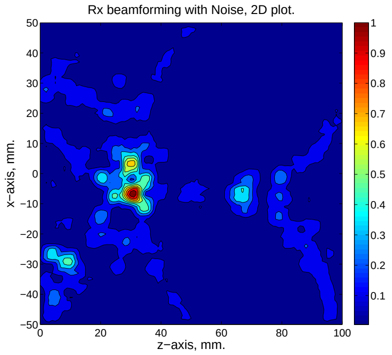

(a) 2D plot for estimating the localization of a tumor at (-7 , 30) with Rx beamforming. The estimated position of the tumor is (-7 , 31).

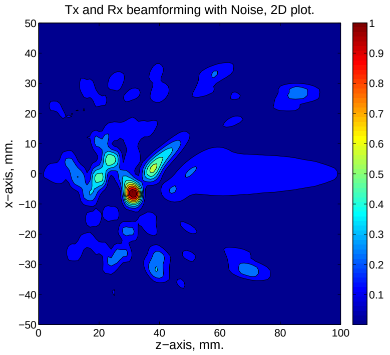

(b) 2D plot for estimating the localization of a tumor at (-7 , 30) with Tx (time corrected) and Rx beamforming. The estimated position of the tumor is (-6 , 31).

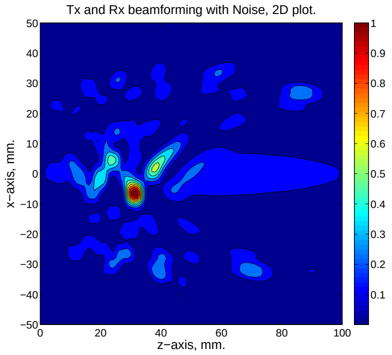

(c) 2D plot for estimating the localization of a tumor at (-7 , 30) with Tx (both time and amplitude corrected) and Rx beamforming. The estimated position of the tumor is (-6 , 31).

Figure 3.14: Maps showing the localization of a tumor at (-7 , 30) with a noise level of $1.0 \cdot 10^{-7}$ added to the signals.

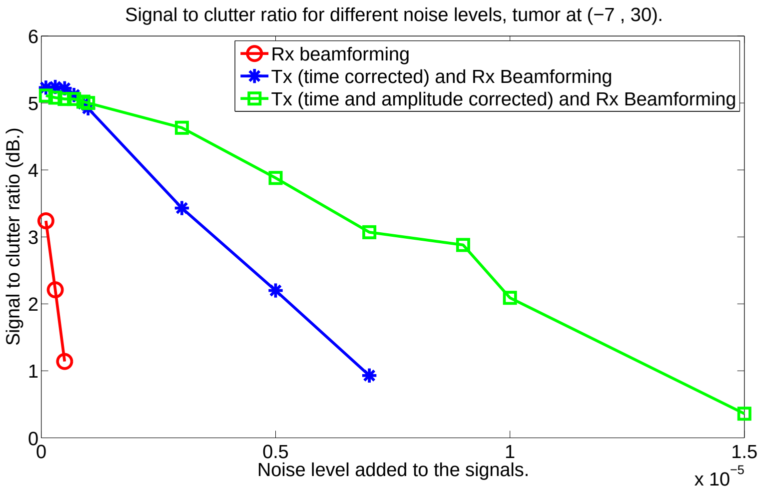

Figure 3.15: The signal-to-clutter ratios when adding different noise levels to the signals and the tumor placed at (-7 , 30).

A tumor was then placed in the extreme localization with coordinates (-35 , 35) as shown on Fig. 2.15(c). The transmitting and receiving methods from the previous models were repeated. The time delays and amplitudes used with the Tx beamforming are listed in Table C.2. The results, after post-processing with a noise level of $1.0 \cdot 10^{-7}$ added, can be seen on Fig. 3.16.

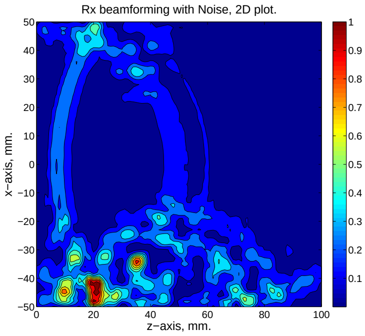

(a) 2D plot for estimating the localization of a tumor at (-35 , 35) with Rx beamforming and no noise added. The estimated position of the tumor is (-42 , 21).

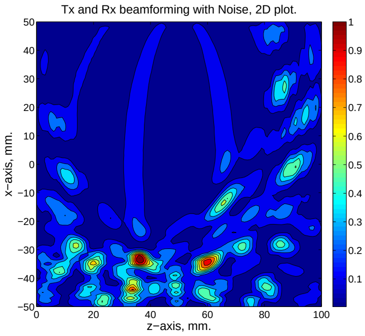

(b) 2D plot for estimating the localization of a tumor at (-35 , 35) with Tx (time corrected) and Rx beamforming. The estimated position of the tumor is (-33 , 36) and a secondary peak is located at (-35 , 60).

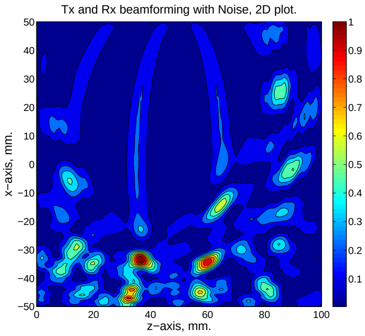

(c) 2D plot for estimating the localization of a tumor at (-35 , 35) with Tx (both time and amplitude corrected) and Rx beamforming. The estimated position of the tumor is (-34 , 37) and a secondary peak is located at (-34 , 60).

Figure 3.16: 2D plots showing the estimated localization of a tumor at (-35 , 35) with a noise level of $1.0 \cdot 10^{-7}$ added to the signals (except where noted).

Tables B.6 and B.7 lists the noise levels, SNR and S/C ratios. No table was made when performing only Rx beamforming because, even without any noise added, the tumor was misplaced as seen on Fig. 3.16(a). The signal-to-clutter ratios as a function of the noise added are presented in Fig. 3.17.

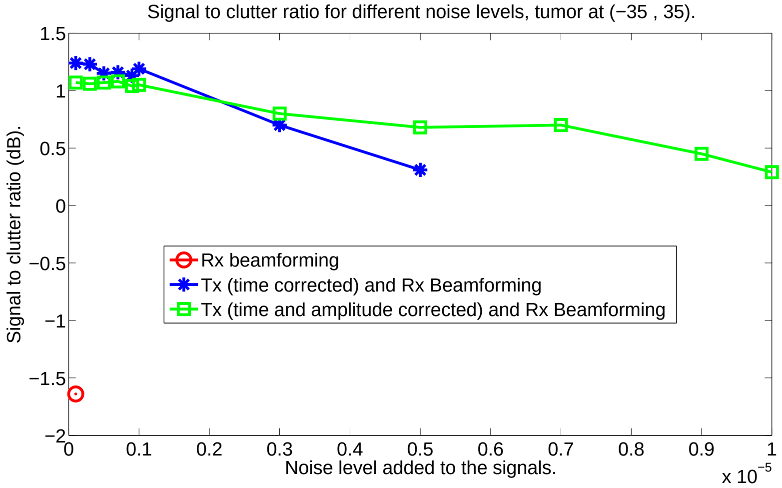

Figure 3.17: The signal-to-clutter ratios when adding different noise levels to the signals and the tumor placed at (-35 , 35).

3.3 Changing model parameters

In addition to studying the systems sensitivity versus changes when adding noise, it is also of interest to determine how the system responds to a change in tumor size. Therefore, the tumor diameter was set to be both 2 mm and 6 mm, in addition to the previous measurements with a diameter of 4 mm. The noise level added was kept constant at $1.0 \cdot 10^{-7}$, and the measurements made with the 4 mm tumor was repeated for the different tumor diameters. The signal-to-clutter ratios are presented in Fig. 3.18.

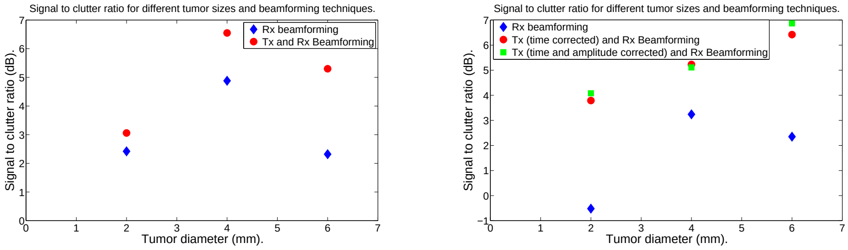

(a) The tumor is placed at (0 , 50). (b) The tumor is placed at (-7 , 30).

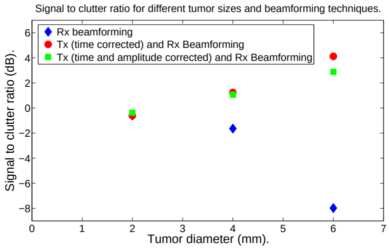

(c) The tumor is placed at (-35 , 35).

Figure 3.18: Signal-to-clutter ratio versus tumor diameter. The noise level added was kept constant at $1.0 \cdot 10^{-7}$ while the diameter of the tumor was varied in steps of 2 mm.

The measurements were repeated, but now the tumor diameter was set to 4 mm, the noise level added was kept constant at $1.0 \cdot 10^{-7}$ and the dielectric constant of the ambient medium, ϵ, was varied. In the previous models, the dielectric constant of the fat was $\epsilon = 10$ thus giving a ratio between the tumor and fat of 5:1. Now, ϵ was set to 20 and 30, making the ratio between the tumor and fat 5:2 and 5:3 respectively. Depending on the content of adipose (fatty) tissue, the range of ϵ varies from about 5-30 in breast tissue [62]. The results from these simulations are presented in Fig. 3.19.

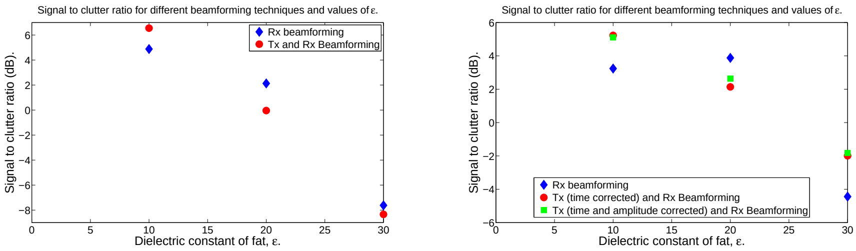

(a) The tumor is placed at (0 , 50). (b) The tumor is placed at (-7 , 30).

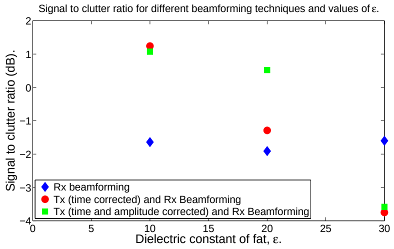

(c) The tumor is placed at (-35 , 35).

Figure 3.19: Signal-to-clutter ratio versus changes in the dielectric constant of the fat. The tumor diameter was set to 4 mm, the dielectric constant of the fat, ϵ, was varied from 10 to 30 in steps of 10. The noise level added was kept constant at $1.0 \cdot 10^{-7}$.

Then, simulations were done in order to establish how sensitive the system was with regard to the active beamforming process on the transmitter. In CST Microwave Studio, field monitors measuring the electric field at the frequencies 2,3,4,5,6,7,8 and 9 GHz where placed in the y=0 plane, the Tx (time and amplitude) beamforming technique was applied to to the three different models and the datas were post-processed. The total electric field was calculated and is presented in Fig. 3.20.

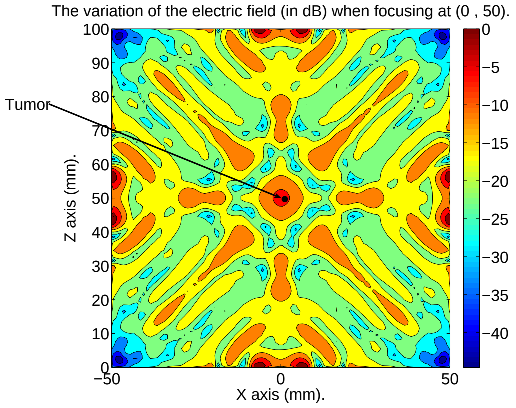

(a) Tx (time and amplitude) beamforming technique used to focus the signals at (0 , 50).

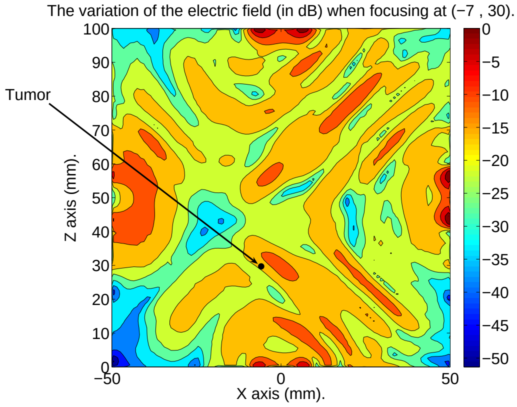

(b) Tx (time and amplitude) beamforming technique used to focus the signals at (-7 , 30).

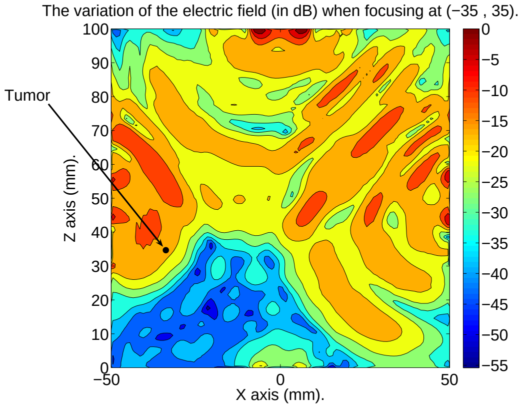

(c) Tx (time and amplitude) beamforming technique used to focus the signals at (-35 , 35).

Figure 3.20: The variations in the electric field when using Tx (time and amplitude corrected) beamforming technique to focus the signals.

Based on the previous figure, Tx (time and amplitude corrected)-Rx beamforming was used to focus the signals 5,10 and 20 mm from the center of the tumor along the positive z direction for each of the three models shown in Fig. 2.15. The signal-to-clutter ratios for these three models are shown in Fig. 3.21.

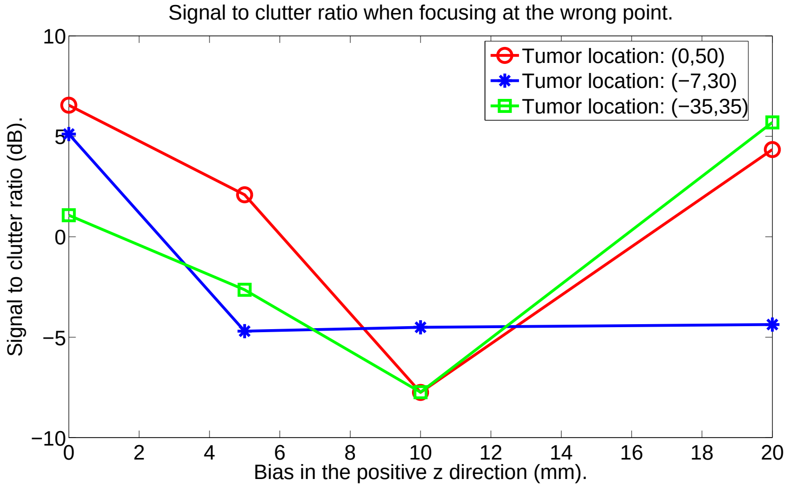

Figure 3.21: The signal-to-clutter ratios when applying Tx (time and amplitude corrected)-Rx beamforming, and focusing the signals 5,10 and 20 mm from the center of the tumor along the positive z direction.

Chapter 4

Discussion

4.1 Antenna characteristics

When changing the different factors in the antenna models, it soon became obvious that the relation between the radius of the outer and inner ellipses was the key factor when trying to improve the magnitude of the S-parameter. In addition, the lumped element, located between the two ellipses at the upper part of the antenna, also affected the S_{11}-parameter. Therefore, one of the first goals in this project was to obtain a magnitude of the S_{11}-parameter below the critical -10 dB point over the largest frequency range possible. Various radii of the ellipses were tested, and the best S-parameter (seen in Fig. 3.1) was found with the configuration shown on Fig. 2.13. This result is comparable with the optimized differential elliptic antenna from [54] and it is somewhat better than the result obtained with the differential elliptic antenna in [61]. These two antennas only uses the 3.1-10.6 GHz band, while the antenna proposed here uses a frequency band that stretches from 1 GHz to 11 GHz.

A verification of the transmitted signal is shown on Fig. 3.2. It is confirmed that the transmitted signal has a Gaussian shape and the values of the 1 GHz and 11 GHz components are about 10 % of the maximum value, when looking at the signal in the frequency domain. Then, the electric field waveforms of the transmitted signal was measured as a function of observation angle at a distance of 50 mm from the antenna. On Fig. 3.3, it is seen clearly that the signal measured in the horisontal plane at 0^o has a larger amplitude than the others and can easily be recognized. However, the amplitude of the signal decrease as the observation angle increase. At the angles 270^o and 90^o, the signal is barely recognizable and has a very low amplitude. In Fig. 3.4, the same angles are used, but now in the vertical x=0 plane. The signal with the largest amplitude is found at 45^o. As the angle increase in either direction from 45^o, the amplitude of the signal decrease. At the most extreme angles, 270^o and 90^o, the signal has a significantly lower amplitude than the one found at 45^o.

The figures showing the fidelity is given in Fig. 3.5 - 3.7. First of all, notice in Fig. 3.5(a), 3.6(a) and 3.7(a) that the x-component of the fidelity is zero along the x=0 plane. This is due to the fact that the x-component of the electric field is zero along this plane and therefore does not contribute. Also, the x-component of the fidelity is always smaller in magnitude than the y- and z- components below y=-5 mm. Below the same line, the y-component seems to be slightly larger than the the z-component. Above y=-5 mm, the x-component is sometimes comparable to the other two components, but never dominates.

Besides this, the mean overall fidelity of 0.8629 is acceptable. This means that, in general, the antenna does not distort the signal significantly before it is radiated. This further implies that the signal generally keeps its shape and duration while being transmitted from the antenna. This is confirmed by the electric field waveforms of the transmitted signal that was measured as a function of observation angle at a distance of 50 mm from the antenna, shown in Figs. 3.3 and 3.4.

The group time delay, shown on Fig. 3.8, has two significant peaks. One peak is located at 5.995 GHz and the other at 8.865 GHz. These peaks can be recognized as local minima at the same frequencies on the magnitude plot of the S_{31}-parameter, shown in Fig. 3.9(a). A plot of the phase of this S-parameter, Fig. 3.9(b), shows a nearly linear phase with the exception of two irregularities located around 6 GHz and 8.9 GHz.

The antenna interpropagation time was found by simulation to be 0.10967 nsec. It was important to establish this parameter, so that it can be removed in later simulations and thus giving a more accurate and correct result when localizing objects at a correct distance.

Looking at the plots of the radiation patterns, it is seen that the x-polarization always has two main lobes located symmetrically on the y axis with respect to the origin. The z-polarization on the other hand, has only one main lobe regardless of the frequency or distance from the antenna. The marked -3 dB levels are significantly wider when moving further out from the antenna, which is confirmed in Tables 3.1 and 3.2. The radiation patterns are stable; there are no large changes in the patterns for the different frequencies or when moving further away from the antenna.

Tables 3.3 and 3.4 list the maximum values of the electric field measured at 10 and 20 mm from the antenna in the calculations of the radiation patterns mentioned above. These maximum values are a measure of how much the different polarizations contribute to the total radiation pattern. The values measured at 10 mm are always higher than the ones measured at 20 mm. This general result is expected since the signal travels through a lossy media. Looking at the values measured at 10 mm, it is seen that the z-polarization dominates at the lowest frequency (1 GHz), the y-polarization at the medium frequencies (3-7 GHz) and the x- and z-polarizations are comparable in strength at the higher frequencies (9 and 11 GHz). This trend is partly confirmed when looking at the values measured at 20 mm from the antenna. Here, the y-polarization also dominates at 9 GHz and the x-polarization is the largest at 11 GHz. In both cases however, the y-polarization is considerably larger than the others at the frequencies 3 and 5 GHz.

A phase center can be difficult to determine, and for this antenna the phase center is confined to an area, shown in Fig. 3.11. If the phase center had been a point, it could have been taken into consideration in the same way as the interpropagation time when estimating distances from the antenna to a tumor. This is obviously more difficult when it is not a point, but lies within an area. Based on the deviation intervals presented in Tables 3.5 and 3.6, an area that was most likely to contain the phase center was established. The maximum deviation expressed as a percentage of the true distance in the x and y direction, was found to be 173.3% and 173% respectively. These extreme deviations may occur because of large angles or due to the presence of the near field exhibited by the radiating antenna. However, according to [63], the conventional phase center concept may be unsuitable for UWB antennas. It is argued that with the use of the standard definition, some UWB antennas might not have a phase center, and that the stable phase center of UWB antennas therefore should be defined as the stability of the phase center in the operating frequency band within the 3 dB beam width.

Placing tumors at different angles and distances from the antenna was the next logical step. As seen in Table 3.7, the estimated distance from the antenna to a tumor are in most cases (except two) equal or shorter than the true distance, which uses the physical origo as a reference point. The maximum deviation in the estimation of distance was found to be 3.9 mm. These results seem promising, especially when taking into consideration that only one antenna was used.

4.2 Antenna beamforming

In the previous section, basic characteristics of the elliptical antenna were established and the distance from one antenna to a tumor was estimated. The antenna interpropagation time was found and will be taken into consideration throughout the rest of the simulations. This section will discuss the expanded model consisting of four identical antennas and one tumor, and the capability of the delay-and-sum beamforming technique applied on the receiver (Rx) and on both the transmitter and receiver (Tx-Rx).

When the tumor was placed at the center with coordinates (0 , 50), its position was correctly estimated when the beamforming was applied to the receiver and on both the receiver and transmitter, assuming a noise level of $1 \cdot 10^{-7}$ added to the signals. This is seen on Fig. 3.12. We also observe that the sidelobe levels are larger in magnitude when beamforming was used only on the receiver, compared to the case with both Tx and Rx beamforming. This is confirmed in Fig. 3.13, where it is shown that the signal-to-clutter ratio is generally higher when applying Tx and Rx beamforming, compared to using it only on the receiver. This figure also shows that when applying Tx and Rx beamforming, the system has a higher tolerance with respect to noise, i.e. it is possible to add more noise to the system and still be able to single out and identify the tumor from the clutter. A maximum noise level of $9 \cdot 10^{-6}$ was added for the Tx and Rx case, while only $1 \cdot 10^{-6}$ for the Rx case.

When placing the tumor at (-7 , 30), see Fig. 3.14, its position was correctly estimated for all three cases of beamforming (when adding a noise level of $1 \cdot 10^{-7}$); only Rx, Tx (time corrected) and Rx, and Tx (time and amplitude corrected) and Rx. However, notice that the sidelobe level is significantly larger when using the Rx beamforming only, resulting in a signal-to-clutter ratio approximately 2 dB lower than in the other two cases, assuming a noise level of $1 \cdot 10^{-7}$. Looking at the signal-to-clutter ratios when adding different noise levels, shown in Fig. 3.15, it is clearly seen that the S/C ratios are much higher in both of the cases when the Tx beamforming is taken into consideration, compared to only using it on the receiver. Comparing the two cases that includes Tx beamforming, the one with only a time correction has a slightly higher signal-to-clutter ratio for low noise levels. But, when the noise level exceeds $7 \cdot 10^{-7}$, the case with both time and amplitude correction has a significantly higher S/C ratio. In addition to this, the beamforming technique has a far better tolerance for noise than the time corrected Tx technique, and is obviously superior to the case where only Rx beamforming was applied.

With the tumor located at (-35 , 35), the Rx beamforming alone was proven to be insufficient for localizing the tumor correctly. It was always estimated to be at a location considerably far away from the true position, even without any noise added to the system. This can clearly be seen in Fig. 3.16(a). When beamforming also was applied on the transmitter, the tumor could be correctly localized, even in the presence of some noise, as seen in Fig. 3.16(b) and (c). Once again, the model with only a time correction on the transmitter has a slightly higher signal-to-clutter ratio for low noise levels. The time and amplitude corrected model, however, has a higher tolerance to noise before it becomes impossible to single out the tumor from the clutter, as shown on Fig. 3.17. The maximum added noise for the time corrected model was $5 \cdot 10^{-5}$, while the time and amplitude corrected one could tolerate a noise level of $1 \cdot 10^{-5}$.

4.3 The effect of changing model parameters

In the three models discussed in the previous section, the beamforming technique itself and the noise level tolerance were emphasized. In order to give a more complete description and a deeper understanding of the strengths of the delay-and-sum beamforming technique applied on the receiver and transmitter, several parameters in the model were altered and the signal-to-clutter ratio was used as a measure of how well the system could handle the changes. In addition to the previously discussed systems tolerance of noise added to the signals, three other parameters that may have an effect of the systems performance were identified and tested, namely the size of the tumor, the difference in dielectric properties of tumor tissue and fat and finally the active beamforming process on the transmitter.

At first, the size of the tumor was changed. In the previous models, the tumor diameter was 4 mm. Now, the same measurements were made with a tumor diameter of 2 mm and 6 mm. The results from the first model, with the tumor at (0 , 50), are presented in Fig. 3.18(a). Here it is seen, as expected, that the S/C ratio is generally lower when using a tumor with a diameter of 2 mm compared to a diameter of 4 mm. However, the model with the 6 mm tumor has a lower S/C ratio than the one with the 4 mm tumor. In fact, when applying only Rx beamforming, the models containing tumors of 2 mm and 6 mm have almost identical S/C ratio, 2.42 dB and 2.32 dB respectively, while with the 4 mm tumor the S/C ratio is larger (4.88 dB). It is also worth noticing that the difference between using only Rx beamforming and using Tx and Rx beamforming increase as the size of the tumor increase.

In the next model, the tumor was placed in (-7 , 30). As seen on Fig. 3.18(b), the 2 mm tumor could not be singled out from the clutter when applying Rx beamforming. When beamforming was applied to the transmitter and the receiver, the tumor was correctly localized and a S/C ratio of approximately 4 dB was obtained for both of these models. The tumors with a diameter of 4 mm and 6 mm were always correctly localized, and the S/C ratios when using Tx and Rx beamforming are always larger than when the beamforming is only performed on the receiver. The difference between the models using the Tx (time corrected) and Tx (time and amplitude corrected) beamforming are barely noticeable.

Fig. 3.18(c) shows the results when placing a tumor at (-35 , 35). For a tumor diameter of 2 mm, it can not be localized correctly even when applying Tx and Rx beamforming. Rx beamforming and tumor diameters of 4 mm and 6 mm gives the same results as with the 2 mm tumor, but when using the delay-and-sum technique on the transmitter, in addition to the receiver, these tumors are identified and localized. The S/C ratios increase as the tumor diameter increase, which is as expected.

For each of the three models the tumor diameter was now set to 4 mm, the noise level added was kept constant at $1.0 \cdot 10^{-7}$ and the dielectric constant of the fat, ϵ, was varied. As seen on Fig. 3.19, the general trend is that the S/C ratios decreases as ϵ increases. This is expected, because it is the difference between the malignant and healthy tissue that is the basis of this method, and when this contrast becomes smaller it will be more difficult to detect the tumor. It is seen that none of the tumors can be detected when the dielectric constant of the fat is set to 30. Furthermore, notice that on Figs. 3.19(a) and (b), the S/C ratios with $\epsilon = 20$, are larger when using Rx beamforming than when applying Tx and Rx beamforming. Looking at Fig. 3.19(c) however, it is seen that the Rx beamforming can not detect the tumor, but the Tx and Rx beamforming technique manages to localize the tumor correctly, at least for ϵ =10 and 20.

We also wanted to test the systems sensitivity with regard to the active beamforming process on the transmitter. In Fig. 3.20, the total electric field when applying Tx (time and amplitude corrected) beamforming is plotted. These plots show a local maximum close to the point in which the signals are focused. This indicates that the energy is focused, but as seen on Figs. 3.20(b) and (c), the maximum is located a few millimeters from the actual focal point. In all of these plots, it is seen that the maximum is stretched out and covers an area. This means that a small deviation in the focal point might not have a large influence on the resulting S/C ratio. To verify this, the focal point was moved with 5,10 and 20 mm in the positive z direction, while the tumor was still placed at the same position as before. The three previous mentioned models were simulated with these new focal points. The Tx (time and amplitude corrected) and Rx beamforming technique was applied and the S/C ratios were found and can be seen in Fig. 3.21. It is seen that as long as the focal point is at a local maximum in Fig. 3.20, the S/C ratio is high. But when the focal point is located elsewhere, the S/C ratio becomes lower than it is when focusing at the center of the tumor.

Chapter 5

Conclusion

An effort has been made to give a general characteristic of this planar elliptical antenna. Initially, I have shown that the antenna has an S_{11}-parameter well below the gold standard -10 dB level over the entire frequency band. In the literature, this parameter is often the first to be established, and it is important to get as much of the frequency band as possible below -10 dB. Then the transmitted signal was documented in both time- and frequency domain, and the 1 GHz and 11 GHz components were found to be approximately 10 percent of the maximum value. This signal was recorded at different angles at a constant distance from the antenna. In general, the signal seems to keep its shape independent of the observation angle, and as the angle increased the amplitude of the signal decreased. This result is supported by a general high fidelity factor and a group time delay that has little variation across the frequency band, except two large peaks at 6.0 GHz and 8.9 GHz. By simulations, the average antenna interpropagation time and phase center was also found. Another more commonly used antenna parameter that was found, was the antenna radiation pattern. The patterns are fairly stable as the frequency increases, and the -3 dB levels are significantly wider when moving further out from the antenna. In addition to these antenna parameters, the distance from one antenna to a tumor, located at different angles and distances, was estimated. These results were acceptable, and the model was expanded to include four antennas and a tumor.

For the models consisting of four antennas and a tumor, the main goal was to test and determine whether there was something to gain when using the delay-and-sum beamforming technique on both the receiver and transmitter. This is confirmed for all three different models that we tested. When applying this beamforming technique on both the receiver and transmitter, the signal-to-clutter ratios are significantly larger than what we get when using the technique on the receiver only. In addition to a higher signal-to-clutter ratio when a low noise level is added to the signals, the system also becomes more tolerant to added noise when using Tx-Rx beamforming, compared to the Rx case.

To examine the strengths of the Tx-Rx beamforming technique more thoroughly, some of the model parameters were changed. When varying the tumor size, it is seen that the S/C ratio is generally higher when using a tumor that is 4 mm in diameter than using one that is 2 mm. The Tx-Rx technique also manages to detect tumors when the Rx beamforming does not succeed. The S/C ratios decreases as the dielectric constant of the fat increases and none of the beamforming methods were able to correctly localize the tumor when the dielectric constant of the fat was $\epsilon = 30$. A somewhat surprising result is that Rx beamforming achieves the highest S/C ratio when $\epsilon = 20$ and the tumor is located at (0 , 50) and (-7 , 30).

When applying Tx-Rx beamforming, there is a local maximum in the electric field close to the desired focal point. We can therefore claim that this technique focuses the energy at the desired location, thus making detection of a tumor more likely. When focusing the signals to a point that is not a local maximum, the signal-to-clutter ratio will become significantly lower and detection of a tumor becomes difficult. This, seen in relation with the other properties mentioned in this chapter, indicates that there is some profit with respect to signal-to-clutter ratio, in applying the Tx-Rx beamforming technique. In many of the models and parameters used and tested here, the Tx-Rx method is equal to or better than the Rx method to detect breast cancer.

Chapter 6

Future work

From my point of view, there are three main areas in which future work should be concentrated. Firstly, a more detailed characteristic of the antenna is needed. Parameters such as gain, current flow on the antenna, radiation efficiency and transfer functions will give a more complete and profound description of the antenna, its limitations and capabilities.

The second area where there is still work to be done, is with regard to the expanded model consisting of four antennas, one tumor and the use of the delay-and-sum beamforming technique. In theory, better results should be obtained with the increase in number of antennas. One possibility will be to add four new antennas to the system, bringing the total number of antennas up to eight. These new antennas could be placed in the corners between the existing antennas, thus covering the area under investigation in a much better way than with the current setup. It is possible to expand this even further and try to localize the tumor in 3 dimensions. This would require that some antennas were placed both above and below the tumor in order to estimate the depth in which the tumor is positioned. The signal processing algorithms will also become more complex as the number of antennas increases.

And finally, the antenna should be produced and tested in order to confirm the antenna characteristics previously found by simulation. Localization of different objects in a medium with similar dielectric properties as fat could also be attempted. The delay-and-sum beamforming technique could also be tested, and try to find out what demands this technique sets to the additional equipment that might be needed.

Appendix A

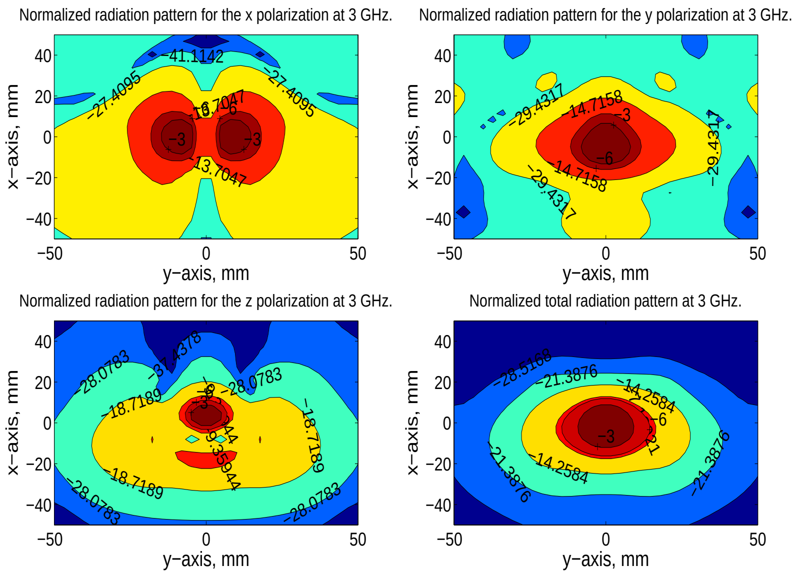

Figure A.1: Radiation pattern measured at the plane z=10mm and at a frequency of 3 GHz. Values are given in dB.

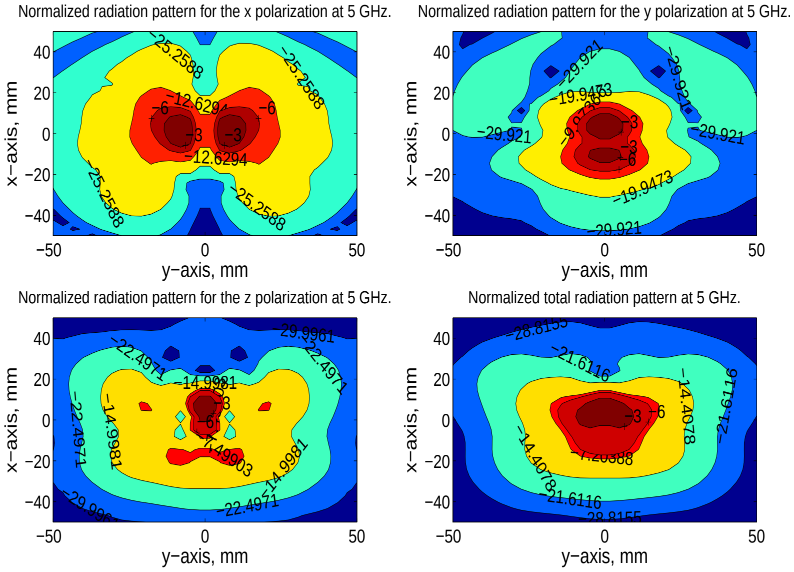

Figure A.2: Radiation pattern measured at the plane z=10mm and at a frequency of 5 GHz. Values are given in dB.

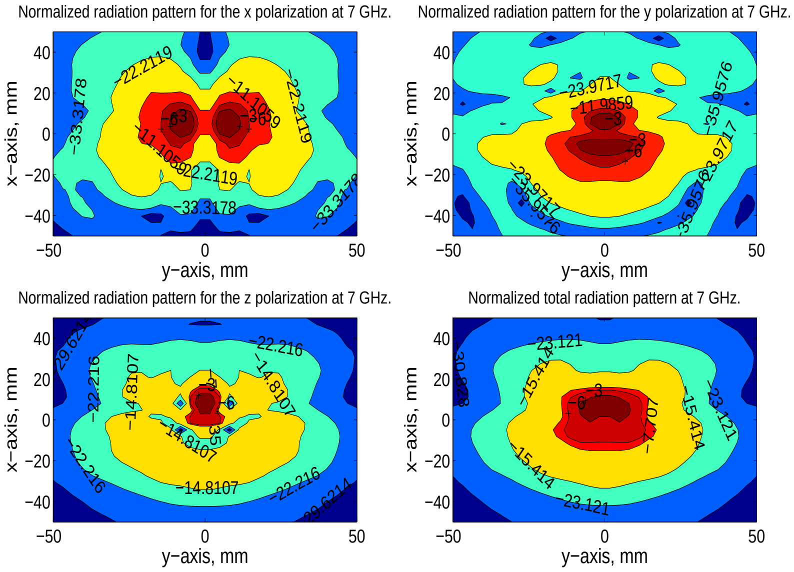

Figure A.3: Radiation pattern measured at the plane z=10mm and at a frequency of 7 GHz. Values are given in dB.

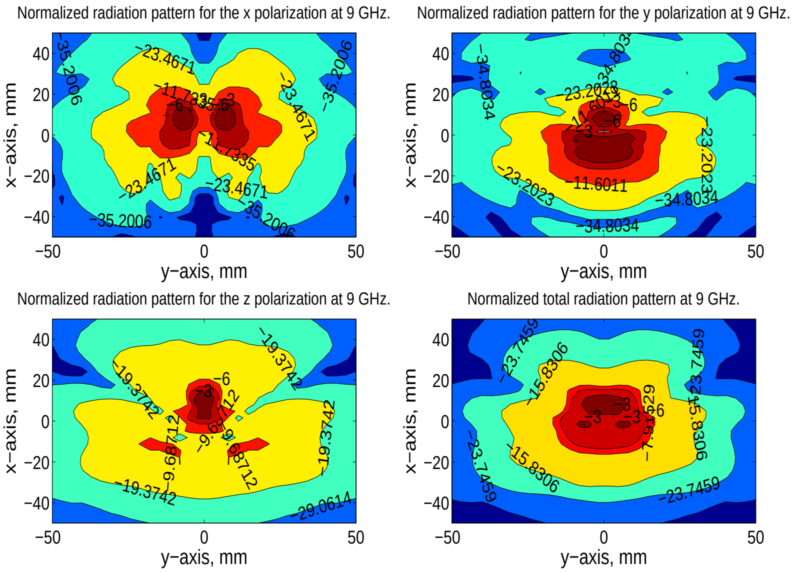
Normalized radiation pattern for the x polarization at 9 GHz.
Normalized radiation pattern for the y polarization at 9 GHz.
Normalized radiation pattern for the z polarization at 9 GHz.
Normalized total radiation pattern at 9 GHz.

Figure A.4: Radiation pattern measured at the plane z=10mm and at a frequency of 9 GHz. Values are given in dB.

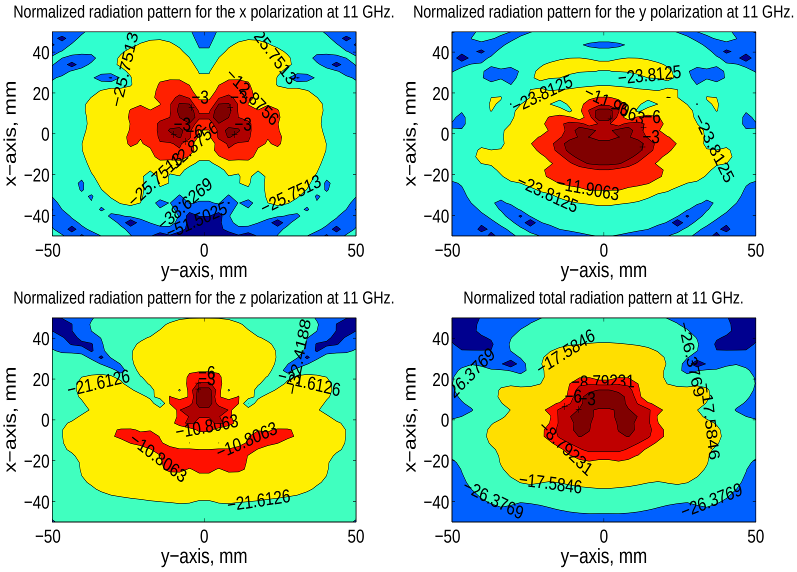
Normalized radiation pattern for the x polarization at 11 GHz.
Normalized radiation pattern for the y polarization at 11 GHz.
Normalized radiation pattern for the z polarization at 11 GHz.
Normalized total radiation pattern at 11 GHz.

Figure A.5: Radiation pattern measured at the plane z=10mm and at a frequency of 11 GHz. Values are given in dB.

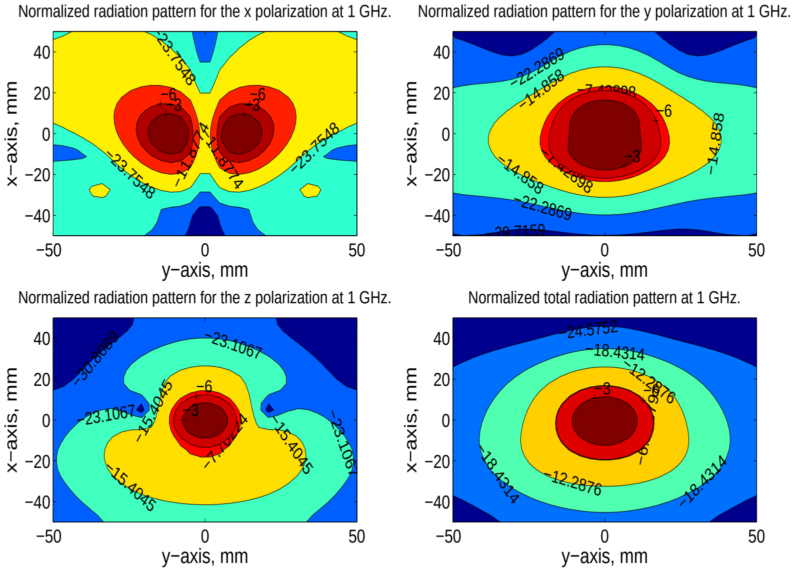

Figure A.6: Radiation pattern measured at the plane z=20mm and at a frequency of 1 GHz. Values are given in dB.

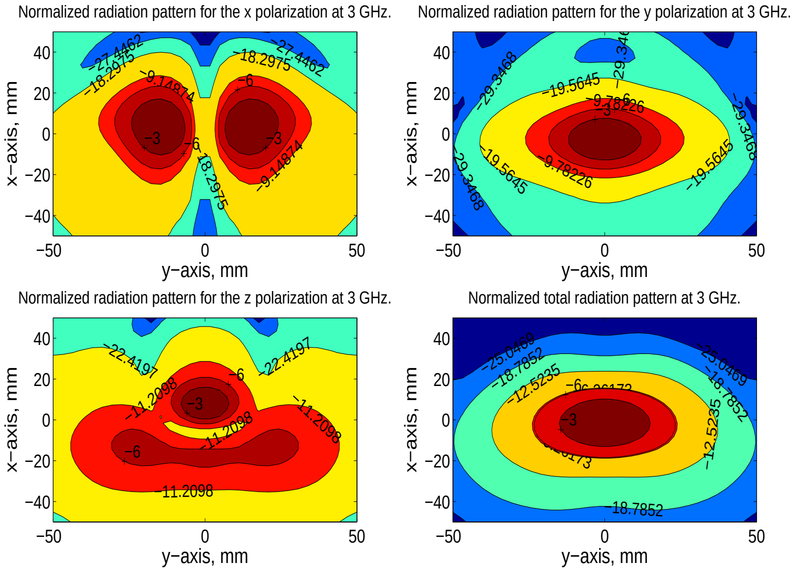

Figure A.7: Radiation pattern measured at the plane z=20mm and at a frequency of 3 GHz. Values are given in dB.

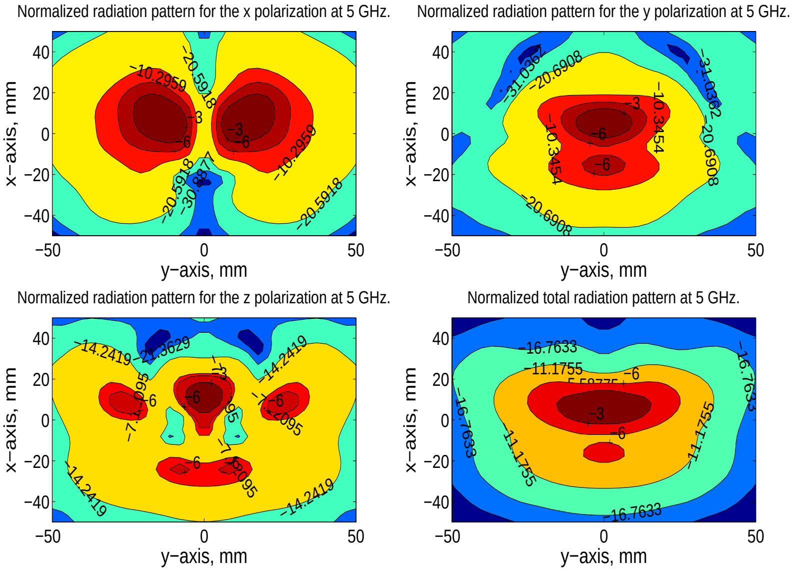

Figure A.8: Radiation pattern measured at the plane z=20mm and at a frequency of 5 GHz. Values are given in dB.

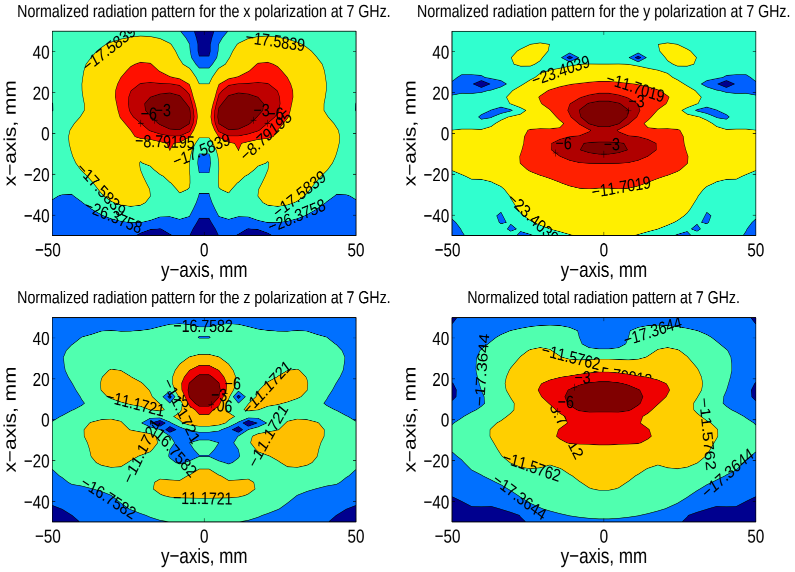

Figure A.9: Radiation pattern measured at the plane z=20mm and at a frequency of 7 GHz. Values are given in dB.

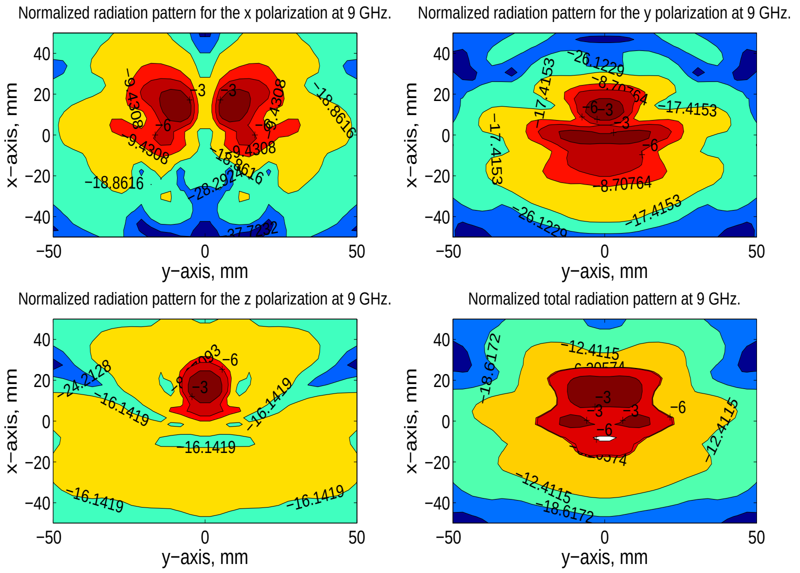

Figure A.10: Radiation pattern measured at the plane z=20mm and at a frequency of 9 GHz. Values are given in dB.

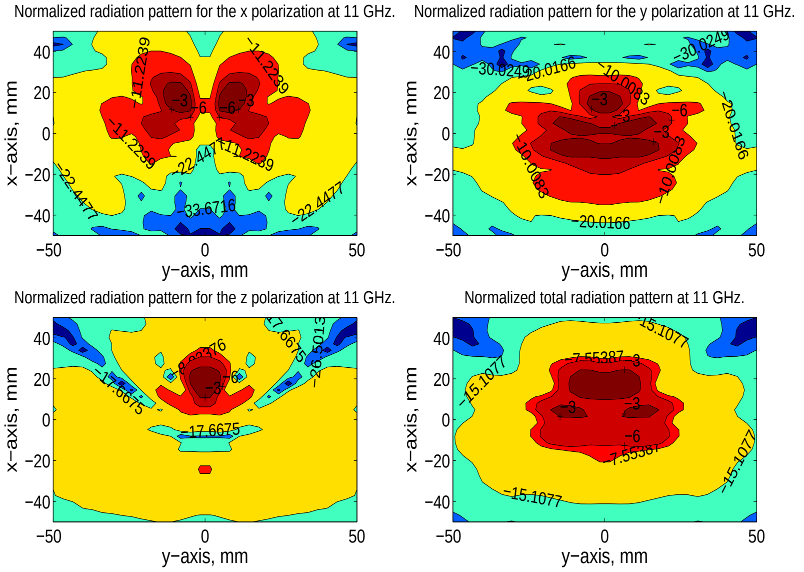

Figure A.11: Radiation pattern measured at the plane z=20mm and at a frequency of 11 GHz. Values are given in dB.

Appendix B

Noise level (10^{-7})	SNR 1 (dB)	SNR 2 (dB)	SNR 3 (dB)	SNR 4(dB)	S/C (dB)
1.0	31.73	31.17	31.14	31.17	4.88
3.0	22.19	21.63	21.60	21.63	4.41
5.0	17.75	17.20	17.16	17.20	3.82
7.0	14.83	14.27	14.24	14.27	3.09
9.0	12.65	12.09	12.06	12.09	2.67
10.0	11.73	11.17	11.14	11.17	2.50

Table B.1: Noise level, SNR of the channels 1-4 and the S/C ratio when the tumor is located at (0 , 50) and Rx beamforming is applied.

Noise level (10^{-7})	SNR 1 (dB)	SNR 2 (dB)	SNR 3 (dB)	SNR 4(dB)	S/C (dB)
1.0	44.90	44.64	44.64	44.64	6.55
3.0	35.35	35.10	35.10	35.10	6.46
5.0	30.92	30.66	30.66	30.66	6.32
7.0	28.00	27.74	27.74	27.74	6.28
9.0	25.81	25.56	25.56	25.56	6.12
10.0	24.90	24.64	24.64	24.64	6.09
30.0	15.35	15.10	15.10	15.10	4.76
50.0	10.92	10.66	10.66	10.66	2.74
70.0	8.00	7.74	7.74	7.74	1.39
90.0	5.81	5.56	5.56	5.56	0.18

Table B.2: Noise level, SNR of the channels 1-4 and the S/C ratio when the tumor is located at (0 , 50) and both Tx and Rx beamforming is applied.

Noise level (10^{-7})	SNR 1 (dB)	SNR 2 (dB)	SNR 3 (dB)	SNR 4(dB)	S/C (dB)
1.0	47.04	24.12	17.17	33.71	3.24
3.0	37.49	14.57	7.63	24.17	2.21
5.0	33.06	10.14	3.19	19.73	1.14

Table B.3: Noise level, SNR of the channels 1-4 and the S/C ratio when the tumor is located at (-7 , 30) and Rx beamforming is applied.

Noise level (10^{-7})	SNR 1 (dB)	SNR 2 (dB)	SNR 3 (dB)	SNR 4(dB)	S/C (dB)
1.0	52.24	41.29	38.47	46.11	5.23
3.0	42.70	31.75	28.93	36.57	5.24
5.0	38.26	27.31	24.49	32.13	5.22
7.0	35.34	24.39	21.57	29.21	5.12
9.0	33.16	22.20	19.38	27.03	4.99
10.0	32.24	21.29	18.47	26.11	4.92
30.0	22.70	11.75	8.93	16.57	3.43
50.0	18.26	7.31	4.49	12.13	2.20
70.0	15.34	4.39	1.57	9.21	0.93

Table B.4: Noise level, SNR of the channels 1-4 and the S/C ratio when the tumor is located at (-7 , 30) and both Tx (time delay) and Rx beamforming is applied.

Noise level (10^{-7})	SNR 1 (dB)	SNR 2 (dB)	SNR 3 (dB)	SNR 4(dB)	S/C (dB)
1.0	59.77	48.20	44.57	53.15	5.11
3.0	50.23	38.66	35.03	43.61	5.08
5.0	45.79	34.22	30.59	39.17	5.06
7.0	42.87	31.30	27.67	36.25	5.06
9.0	40.69	29.12	25.48	34.07	5.02
10.0	39.77	28.20	24.57	33.15	5.00
30.0	30.23	18.66	15.03	23.61	4.63
50.0	25.79	14.22	10.59	19.17	3.88
70.0	22.87	11.30	7.67	16.25	3.07
90.0	20.69	9.12	5.48	14.07	2.88
100.0	19.77	8.20	4.57	13.15	2.09
150.0	16.25	4.68	1.05	9.63	0.36

Table B.5: Noise level, SNR of the channels 1-4 and the S/C ratio when the tumor is located at (-7 , 30) and both Tx (time delay and amplitude corrected) and Rx beamforming is applied.

Noise level (10^{-7})	SNR 1 (dB)	SNR 2 (dB)	SNR 3 (dB)	SNR 4(dB)	S/C (dB)
1.0	55.01	37.75	39.39	63.07	1.24
3.0	45.47	28.21	29.85	53.53	1.23
5.0	41.03	23.77	25.41	49.09	1.15
7.0	38.11	20.85	22.49	46.17	1.16
9.0	35.93	18.67	20.31	43.99	1.13
10.0	35.01	17.75	19.39	43.07	1.19
30.0	25.47	8.21	9.85	33.53	0.70
50.0	21.03	3.77	5.41	29.09	0.31

Table B.6: Noise level, SNR of the channels 1-4 and the S/C ratio when the tumor is located at (-35 , 35) and both Tx (time delay) and Rx beamforming is applied.

Noise level (10^{-7})	SNR 1 (dB)	SNR 2 (dB)	SNR 3 (dB)	SNR 4(dB)	S/C (dB)
1.0	62.36	47.90	51.44	74.15	1.07
3.0	52.81	38.35	41.90	64.61	1.06
5.0	48.38	33.92	37.46	60.17	1.07
7.0	45.45	31.00	34.54	57.25	1.08
9.0	43.27	28.81	32.36	55.07	1.04
10.0	42.36	27.90	31.44	54.15	1.05
30.0	32.81	18.35	21.90	44.61	0.80
50.0	28.38	13.92	17.46	40.17	0.68
70.0	25.45	11.00	14.54	37.25	0.70
90.0	23.27	8.81	12.36	35.07	0.45
100.0	22.36	7.90	11.44	34.15	0.29

Table B.7: Noise level, SNR of the channels 1-4 and the S/C ratio when the tumor is located at (-35 , 35) and both Tx (time delay and amplitude corrected) and Rx beamforming is applied.

Appendix C

Antenna Number	Time Delay (ns)	Amplitude
3	0.0	6.0243
2	0.1047997	3.8031
4	0.241656	2.1489
1	0.4168228	1.0

Table C.1: Transmitting sequence, time delay and amplitude of the four antennas when the tumor is placed at (-7 , 30).

Antenna Number	Time Delay (ns)	Amplitude
2	0.0	21.7445
3	0.13165	14.0270
1	0.38807	4.6853
4	0.68622	1.0

Table C.2: Transmitting sequence, time delay and amplitude of the four antennas when the tumor is placed at (-35 , 35).

Bibliography

[1] Bjålie, J. G., E. Haug, O. Sand, and Ø. V. Sjaastad, "Menneskekroppen-Fysiologi og anatomi," Fourth Edition, 2001.

[2] "National Cancer Institute - Stages of Breast cancer," http://www.cancer.gov/cancertopics/pdq/treatment/breast/Patient/page2, 02/15/2007.

[3] "Imaginis-Staging and Survival Rates of Breast Cancer," http://www.imaginis.com/breasthealth/staging_print.asp, 20/02/2008.

[4] Orel, S. G., and R. H. Troupin, "Nonmammographic imaging of the breast: current issues and future prospects," *Semin Roentgenol* Vol.28, pp.231-241, 1993.

[5] Hendee, W. R., and E. R. Ritenour, "Medical Imaging Physics," Fourth Edition, 2002.

[6] Huynh, P. T., A. M. Jarolimek, and S. Daye, "The false-negative mammogram," *Radiograph.*, vol 18, no 5, pp.1137-1154, 1998.

[7] Elmore, J. G., M. B. Barton, V. M. Moceri, S. Polk, P. J. Arena, and S. W. Fletcher, "Ten-year risk of false positive screening mammograms and clinical breast examinations," *New Eng. J. Med.,* vol.338, no16, pp.1089-1096, 1998.

[8] Silverstein, M. J., E. D. Gierson, P. Gamagami, et al. "Breast cancer diagnosis in women augmented with silicone gel-filled implants," *Cancer.* Vol.66, pp.97-101, 1990.

[9] Sehgal, C. M., S. P. Weinstein, P. H. Arger, and E. F. Conant, "A Review of Breast Ultrasound," *J Mammary Gland Biol Neoplasia,* Vol. 11, pp. 113-123, 2006.

[10] Ferris, C. F., M. Febo, F. Luo, K. Schmidt, M. Brevard, J. A. Harder, P. Kulkarni, T. Messenger, and J. A. King, "Functional Magnetic Resonance Imaging in Conscious Animals: A New Tool in Behavioural Neuroscience Research," *Journal of Neuroendocrinology,* Vol. 18, pp. 307Ű318, 2006.

[11] Orel, S. G., M. D. Schnall, V. A. LiVolsi, et al. "Suspicious breast lesions: MR imaging with radiologic-pathologic correlation," *Radiology* Vol.190, pp.485-493, 1994.

[12] Kuhl, C. K., R. K. Schmutzler, C. C Leutner, et al. "Breast MR imaging screening in 192 women proved or suspected to be carriers of a breast cancer susceptibility gene: preliminary results," *Radiology* Vol.215, pp.267-279, 2000.

[13] Orel, S. G., "MR imaging of the breast," *Radiol Clin North Am.* Vol.38, pp.899-913, 2000.

[14] Orel, S. G., and M. D. Schnall, "MR Imaging of the Breast for the Detection, Diagnosis, and Staging of Breast Cancer," *Radiology,* Vol.220, No.1, pp.13-30, 2001.

[15] Federal Communications Commission, First Report and Order, Revision of Part 15 of the Commission's Rules Regarding Ultra-Wideband Transmission Systems, FCC 02-48, April 22, 2002.

[16] Daniels, D. J., "Surface-Penetrating Radar," London, IEE Press, 1996.

[17] Li, X., E. j. Bond, B. D. Van Veen, and S. C. Hagness, "An overview of Ultra-Wideband Microwave Imaging via Space-Time Beamforming for Early-Stage Breast-Cancer Detection," *IEEE Antennas and Propagation Magazine,* Vol. 47, No. 1, February 2005.

[18] Chaudhary, S. S., R. K. Mishra, A. Swarup, and J. M. Thomas, "Dielectric Properties of Normal and Malignant Human Breast Tissues at Radiowave and Microwave Frequencies," *Indian J. Biochem. and Biophys.,* vol. 21, pp. 76-79, February 1984.

[19] Surowiec, A. J., S. S. Stuchly, J. R. Barr, and A. Swarup, "Dielectric Properties of Breast Carcinoma and the Surrounding Tissues," *IEEE Transactions on Biomedical Engineering,*vol. 35, pp. 257-263, April 1988.

[20] Joines, W. T., Y. Z. Dhenxing, and R. L. Jirtle, “The Measured Electrical Properties of Normal and Malignant Human Tissues from 50 to 900 MHz,” *Med. Phys.,*vol. 21, pp. 547-550, April 1994.

[21] Kruger, R. A., K. K. Kopecky, A. M. Aisen, D. R. Reinecke, G. A. Kruger, and W. L. Kiser, Jr., “Thermoacoustic CT with radio waves: A medical imaging paradigm,” *Radiology,* vol. 211, pp. 275Ű278, 1999.

[22] Wang, L. V., X. Zho, H. Sun, and G. Ku, “Microwave-induced acoustic imaging of biological tissues,” *Rev. Sci. Instrum.,* vol. 70, pp. 3744Ű3748, 1999.

[23] Meaney, P. M. and K. D. Paulsen, “Nonactive antenna compensation for fixed-array microwave imaging: Part IIŮImaging results,” *IEEE Trans. Med. Imag.,* vol. 18, pp. 508Ű518, June 1999.

[24] Meaney, P. M., M. W. Fanning, D. Li, S. P. Poplack, and K. D. Paulsen, “A clinical prototype for active microwave imaging of the breast,” *IEEE Trans. Microwave Theory Tech.,* vol. 48, pp. 1841Ű1853, November 2000.

[25] Souvorov, A. E., A. E. Bulyshev, S. Y. Semenov, R. H. Svenson, and G. P. Tatsis, “Two-dimensional computer analysis of a microwave flat antenna array for breast cancer tomography,” *IEEE Trans. Microwave Theory Tech.,* vol. 48, pp. 1413Ű1415, August 2000.

[26] Bulyshev, A. E., S. Y. Semenov, A. E. Souvorov, R. H. Svenson, A. G. Nazarov, Y. E. Sizov, and G. P. Tatsis, “Computational Modeling of Three-Dimensional Microwave Tomography of Breast Cancer,” *IEEE Transactions on Biomedical Engineering,* Vol. 48, No. 9, pp. 1053-1056, September 2001.

[27] Liu, Q. H., Z. Q. Zhang, T. T. Wang, J. A. Bryan, G. A. Ybarra, L. W. Nolte, and W. T. Joines, “Active microwave imaging IŮ2-D forward and inverse scattering methods,” *IEEE Trans. Microwave Theory Tech.,* vol. 50, pp. 123Ű133, January 2002.

[28] Hagness, S. C., A. Taflove, and J. E. Bridges, “Two-dimensional FDTD analysis of a pulsed microwave confocal system for breast cancer detection: Fixed-focus and antenna-array sensors,” *IEEE Trans. Biomed. Eng.,* vol. 45, pp. 1470Ű1479, December 1998.

[29] Hagness, S. C., A. Taflove, and J. E. Bridges, “Three-dimensional FDTD analysis of a pulsed microwave confocal system for breast cancer detection: Design of an antenna-array element,” *IEEE Trans. Antennas Propagat.,* vol. 47, pp. 783Ű791, May 1999.

[30] Li, X. and S. C. Hagness, “A confocal microwave imaging algorithm for breast cancer detection,” *IEEE Microwave Wireless Comp. Lett.,* vol. 11, pp. 130Ű132, March 2001.

[31] Fear, E. C. and M. A. Stuchly, “Microwave detection of breast cancer,” *IEEE Trans. Microwave Theory Tech.,* vol. 48, pp. 1854Ű1863, November 2000.

[32] Fear, E. C., X. Li, S. C. Hagness, and M. Stuchly, “Confocal microwave imaging for breast cancer detection: Localization of tumors in three dimensions,” *IEEE Trans. Biomed. Eng.,* vol. 49, pp. 812Ű822, August 2002.

[33] Bond, E. J., X. Li, S. C. Hagness, and B. D. Van Veen, “Microwave imaging via spaceŰtime beamforming for early detection of breast cancer,” *IEEE Trans. Antennas Propagat.,* vol. 51, pp. 1690Ű1705, August 2003.

[34] Davis, S. K., E. J. Bond, X. Li, S. C. Hagness, and B. D. Van Veen, “Microwave imaging via spaceŰtime beamforming for early-stage breast cancer detection: Beamformer design in the frequency domain,” *J. Electromagn. Waves Applicat.,* vol. 17, no. 2, pp. 357Ű381, 2003.

[35] Li, X., S. K. Davis, S. C. Hagness, D. van der Weide, and B. D. Van Veen, “Microwave Imaging via Space-Time Beamforming: Experimental Investigation of Tumor Detection in Multilayer Breast Phantoms,” *IEEE Trans. Microwave Theory Tech.,* vol. 52, No. 8, August 2004.

[36] Zhang, Z. Q., Q. Liu, C. Xiao, E. Ward, G. Ybarra, and W. T. Joines, “Microwave Breast Imaging: 3-D Forward Scattering Simulation,” *IEEE Transactions on Biomedical Engineering,* Vol. 50, No. 10, pp. 1180-1189, 2003.

[37] Li, X., S. C. Hagness, B. D. Van Veen, and D. van der Weide, “Experimental Investigation of Microwave Imaging via Space-Time Beamforming for Breast Cancer Detection,” In 2003 IEEE MTT-S International Microwave Symposium Digest, Jun 8-13 2003, 1, 379-382.

[38] Pozar, D. M., “Microwave Engineering” Third Edition, 2005.

[39] Balanis, C. A., "Advanced Engineering Electromagnetics" 1989.

[40] Bently, J. P., "Principles of Measurement Systems" Fourth Edition, 2005.

[41] Zhang, K., and D. Li, "Electromagnetic Theory for Microwaves and Optoelectronics," Springer-Verlag Berlin Heidelberg 1998.

[42] Deschamps, G. A., "Microstrip Microwave Antennas," *Proc. 3rd USAF Symposium on Antennas,* 1953.

[43] Munson, R. E., "Single Slot Cavity Antennas Assembly," U.S. Patent No.3713162, January 23, 1973.

[44] Munson, R. E., "Conformal Microstrip Antennas and Microstrip Phased Arrays," *IEEE Trans. Antennas Propagation,* Vol. AP-22, pp. 74-78, 1974.

[45] Howell, J. Q., "Microstrip Antennas," *IEEE Trans. Antennas Propagation,* Vol. AP-23, pp. 90-93, 1975.

[46] Kumar, G., and K. P. Ray, "Broadband Microstrip Antennas," Artech House, Inc., 2003.

[47] Maxwell, J. C., "A Treatise on Electricity and Magnetism," Oxford University Press, London, UK, 1873, 1904.

[48] Balanis, C. A., "Antenna Theory: Analysis and Design" Third Edition, 2005.

[49] Johnson, R. C., "Antenna Engineering Handbook" Third Edition.

[50] IEEE, "IEEE Standard Definition of Terms for Antennas," IEEE Std. 145-1993, Institute for Electrical and Electronics Engineers, Inc., New York, NY, USA, March 1993.

[51] Best, S. R., "Distance-Measurement error Associated with Antenna Phase-Center Displacement in Time-Reference Radio Positioning Systems," *IEEE Antennas and Propagation Magazine,* Vol.46, No.2, April 2004.

[52] Blake, L. V., "Antennas," Second Edition, 1984.

[53] Qing, X., Z. N. Chen, and M. Y. W. Chia (2006), "Characterization of ultrawideband antennas using transfer functions," *Radio Sci., 41,* RS1002, doi:10.1029/2005RS003287.

[54] Telzhensky, N., and Y. Leviatan, "Planar Differential Elliptical UWB Antenna Optimization," *IEEE Transactions on antennas and propagation,* Vol.54, No.11, November 2006.

[55] Ghannoum, H., S. Bories, and R. DŠ Errico, "Small-size UWB Planar Antenna and its Behaviour in WBAN/WPAN Applications," *IEE Symposium on Ultra Wideband Systems, Technologies and Applications,* London, 20th April 2006.

[56] Mohammadian, A. H., A. Rajkotia., and S. S. Soliman, "Characterization of UWB Transmit-Receive Antenna System," *IEEE Conference on Ultra Wideband Systems and Technologies,* pp. 157-161, 2003.

[57] Bixian, L., and L. Jian, "Measurement of group delay at ns level precision in exterior ballistic measurements," *National Air Intelligence Center,* NAIC-ID(RS)T-0083-96, 17th May 1996.

[58] Weiland, T., "A discretization method for the solution of Maxwell's equations for six-component fields," *Electronics and Communication, (AEÜ),* Vol.31, pp. 116-120, 1977.

[59] Zhang, H., J. Zhang, and H. Zhang, "Numerical predictions for radar absorbing silicon carbide foams using a finite integration technique with a perfect boundary approximation," *Smart Mater. Struct.,* Vol.15, pp.759-766(8), 2006.

[60] "CST MICROWAVE STUDIO ®4 - Advanced Topics," pp.27-31, 2002.

[61] Powell, J., and A. Chandrakasan, "Differential and Single Ended Elliptical Antennas for 3.1-10.6 GHz Ultra Wideband Communication," *Antennas and Propagation Society International Symposium,* Vol.3, pp. 2935-2938, June 2004.

[62] Lazebnik, M., D. Popovic, L. McCartney, C. B. Watkins, M. J. Lindstrom, J. Harter, S. Sewall, T. Ogilvie, A. Magliocco, T. M. Breslin, W. Temple, D. Mew, J. H. Booske, M. Okoniewski, and S. C. Hagness, "A large-scale study of the ultrawideband microwave dielectric properties of normal, benign, and malignant breast tissues obtained from cancer surgeries," *Physics in Medicine and Biology,* vol. 52, pp. 6093-6115, 2007.

[63] Wu, Q., Bo-shi Jin, L. Bian, Yu-ming Wu, and Le-Wei Li, "An approach to the determination of the phase center of Vivaldi-based UWB antenna," *Antennas and Propagation Society International Symposium 2006, IEEE,* pp. 563-566, 9-14 July 2006.